NASA/TM–20250009190

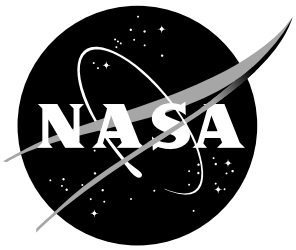

Aerodynamic and Acoustic Characterization of a Ducted Propeller in a Small Hover Anechoic Chamber

Nikolas S. Zawodny, Noah H. Schiller, Nicole A. Pettingill
Langley Research Center, Hampton, Virginia

Glenn L. Medina
Marshall Space Flight Center, Huntsville, Alabama

September 2025

NASA STI Program. . . in Profile

Since its founding, NASA has been dedicated to the advancement of aeronautics and space science. The NASA scientific and technical information (STI) program plays a key part in helping NASA maintain this important role.

The NASA STI Program operates under the auspices of the Agency Chief Information Officer. It collects, organizes, provides for archiving, and disseminates NASA's STI. The NASA STI Program provides access to the NASA Aeronautics and Space Database and its public interface, the NASA Technical Report Server, thus providing one of the largest collection of aeronautical and space science STI in the world. Results are published in both non-NASA channels and by NASA in the NASA STI Report Series, which includes the following report types:

- TECHNICAL PUBLICATION. Reports of completed research or a major significant phase of research that present the results of NASA programs and include extensive data or theoretical analysis. Includes compilations of significant scientific and technical data and information deemed to be of continuing reference value. NASA counterpart of peer-reviewed formal professional papers, but having less stringent limitations on manuscript length and extent of graphic presentations.
- TECHNICAL MEMORANDUM. Scientific and technical findings that are preliminary or of specialized interest, e.g., quick release reports, working papers, and bibliographies that contain minimal annotation. Does not contain extensive analysis.
- CONTRACTOR REPORT. Scientific and technical findings by NASA-sponsored contractors and grantees.
- CONFERENCE PUBLICATION. Collected papers from scientific and technical conferences, symposia, seminars, or other meetings sponsored or co-sponsored by NASA.
- SPECIAL PUBLICATION. Scientific, technical, or historical information from NASA programs, projects, and missions, often concerned with subjects having substantial public interest.
- TECHNICAL TRANSLATION. English-language translations of foreign scientific and technical material pertinent to NASA's mission.

Specialized services also include organizing and publishing research results, distributing specialized research announcements and feeds, providing information desk and personal search support, and enabling data exchange services.

For more information about the NASA STI Program, see the following:

- Access the NASA STI program home page at `http://www.sti.nasa.gov`
- E-mail your question to `help@sti.nasa.gov`
- Phone the NASA STI Information Desk at 757-864-9658
- Write to:
  NASA STI Information Desk
  Mail Stop 148
  NASA Langley Research Center
  Hampton, VA 23681-2199

NASA/TM–20250009190

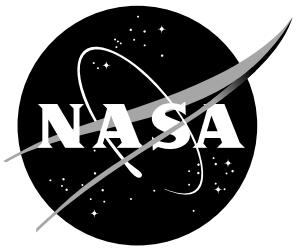

Aerodynamic and Acoustic Characterization of a Ducted Propeller in a Small Hover Anechoic Chamber

Nikolas S. Zawodny, Noah H. Schiller, Nicole A. Pettingill
Langley Research Center, Hampton, Virginia

Glenn L. Medina
Marshall Space Flight Center, Huntsville, Alabama

National Aeronautics and
Space Administration

Langley Research Center
Hampton, Virginia 23681-2199

September 2025

Acknowledgments

The authors would like to acknowledge Matthew Galles of the Applied Acoustics Branch at NASA Langley Research Center for laying the mechanical design groundwork for this effort. The authors would also like to acknowledge John Swartzbaugh and Bryan Lamb of the NASA Langley Jet Noise Laboratory for their assistance in facility setup and debugging. Funding for this effort was provided by the NASA Revolutionary Vertical Lift Technology (RVLT) project.

Available from:

NASA STI Program / Mail Stop 148
NASA Langley Research Center
Hampton, VA 23681-2199
Fax: 757-864-6500

Abstract

This study investigates the aerodynamic performance and acoustic characteristics of a sub-scale ducted propeller relative to an open propeller of common geometry for static hover and low-speed axial flow conditions. The propeller test article is a four-bladed modified optimum hovering rotor, while the duct consists of a blended geometry between a referenced leading edge design and a NACA 0018 trailing edge. Low-fidelity modeling tools are leveraged to provide a predictive comparison for both isolated and ducted propeller systems. The ANOPP-PAS code was found to model the fundamental acoustic blade passage frequency directivity of the isolated propeller quite well, with adjustments made to the simulation case to account for additional torque loading believed to be due to "over-tripping" of the blades. Both momentum theory and the Ducted Fan Design Code yielded good agreement with the measured thrust levels of the ducted propeller system in hover, with the latter prediction method showing good agreement for low-speed axial flow conditions as well. These good agreements, however, were limited to the higher tested propeller rotation rates. Overall, the ducted propeller exhibited slightly improved propulsive efficiency in hover, and poorer efficiency in low-speed axial flow relative to the isolated propeller. Acoustically, the ducted configuration was seen to exhibit acoustic shielding at the propeller blade passage frequency, however an increase in higher blade passage frequency harmonics was also observed. There was also an increase in measured broadband noise associated with the incorporation of the duct, which was more prevalent for the hover operating conditions.

Contents

1 Introduction

New aircraft are being developed to enable local operations including passenger transport, cargo delivery, and emergency response. While the number of Advanced Air Mobility (AAM) missions are projected to increase over the next decade, the environmental impact could limit high density operations. Many proposed AAM aircraft are electric, which reduces concerns about emissions, but noise remains an important issue particularly for local operations in and around communities.

While the current generation of AAM vehicles is diverse, most rely on unducted propulsors. The choice of ducted versus unducted configurations involves a trade-off between noise and performance. Ducted configurations, for example, have the potential to reduce noise but increase the weight and drag of the vehicle [1, 2]. An illustration of such a ducted vehicle configuration is the NASA Revolutionary Vertical Lift Technology (RVLT) *Tiltduct Reference Vehicle for Urban Air Mobility* [2], which is illustrated in Fig. 1. As this figure shows, this vehicle concept is intended to operate across a range of flight conditions encompassing vertical takeoff and landing (VTOL), axial forward flight, and the transition envelope between these conditions. As the name implies, the ability of the vehicle to operate across this wide range of flight conditions is achieved by physical articulation (or tilting) of the propulsors.

(a) VTOL condition (b) Axial forward flight condition

Figure 1. Renderings of the NASA RVLT Tiltduct reference vehicle concept in (a) VTOL and (b) axial forward flight configurations.

As the market matures and the tempo of operations increases, the relative importance of different design requirements could change. Having accurate models to predict tradeoffs for ducted configurations may be important to inform the design of the next generation of AAM vehicles. Specifically, models are needed to capture duct aerodynamics, duct acoustic propagation and scattering, and the impact of acoustic liners in the duct. While some models and data are available, particularly aerodynamic data from the 1960s [3–5], there is generally a lack of high-quality acoustic data for relevant ducted configurations that include acoustic liners in the duct. There has been a lot of work to characterize and improve the acoustic performance of liners for larger turbofan aircraft [6, 7], but it is not clear if the data and models are applicable to AAM vehicles with shorter ducts, lower solidity propellers,

and lower tip speeds. Lower Mach number, non-axial inflow will also be more important on AAM vehicles with transitional flight conditions than on conventional turbofan aircraft.

This paper documents the aerodynamic and acoustic characterization of a small, ducted propeller. This paper documents the first test in a series that evaluates increasingly larger scales that are more representative of full-scale AAM configurations. The duct considered in this test has a 10" inner diameter without stators or acoustic treatment. In addition, the flow conditions are limited to static and low-speed axial inflow. More details concerning the experimental setup, including a description of the duct, propeller, facility, and test matrix, are included in the following section. Two different modeling approaches are then described, which were used to assess the design and help interpret the experimental results. Both aerodynamic and acoustic results are then presented and compared. Finally, some concluding remarks are provided.

2 Experimental Setup

2.1 Test Articles

The two test articles used in this study are a four-bladed propeller, and a circular duct that encapsulates the propeller. The following sections discuss the design and fabrication details of these test articles.

2.1.1 Propeller Design

The propeller designed for this investigation is a four-bladed optimum hovering rotor. An optimum hovering rotor is one that has both minimal induced and profile power requirements according to blade element momentum theory (BEMT) [8]. The twist distribution along the rotor blade is designed to produce uniform inflow over the blade span, to which the minimal induced power is attributed. This twist distribution, $\Theta_{tw}(r)$, is of the form

$$\Theta_{tw}(r) = \frac{R}{r}\left(\frac{4C_{T_{\text{design}}}}{C_{l,\alpha}\sigma(r)} + \sqrt{\frac{C_{T_{\text{design}}}}{2}}\right) - \alpha_0, \tag{1}$$

where r is the spanwise station along the blade (from blade root 0 to blade radius R), $C_{T_{\text{design}}}$ is the desired rotor thrust coefficient, $C_{l,\alpha}$ is the airfoil lift curve slope, $\sigma(r)$ is the spanwise distribution of solidity, and α_0 is the zero-lift angle of attack of the airfoil. The rotor thrust coefficient and solidity are further defined as

$$C_T = \frac{T}{\rho_\infty A \Omega^2 R^2}, \tag{2}$$

and

$$\sigma(r) = \frac{N_b\, c(r)}{\pi R}, \tag{3}$$

where N_b is the number of rotor blades, and $c(r)$ is the blade chord distribution along the span. Furthermore, an optimum hovering rotor has a tapered chord distribution of the form

$$c(r) = \frac{c_{\text{tip}}}{r/R}, \tag{4}$$

where c_{tip} is the chord length at the blade tip. This chord distribution allows for each radial station to operate at an optimal lift-to-drag ratio, to which the minimal profile power condition is attributed. This $1/r$ type of taper distribution is typically impractical to manufacture; however, a common practice is to replace the $1/r$ taper distribution with a linear taper distribution because it well approximates the $1/r$ distribution for the outboard spanwise regions of the blade radius.

Figure 2 provides the blade angles and chord distributions of the rotor blade tested in this study. As shown in Fig. 2(a), the blade twist and induced flow angle distributions obey a $1/r$ roll-off trend, while the design angle of attack distribution is a constant value of $\alpha_{\text{design}} = 3.25°$. Furthermore, Fig. 2(b) shows the optimum chord distribution according to Eq. 4, as well as a simplified linear chord distribution using a 2.5:1 taper ratio. This taper ratio is seen to overlay very closely with the

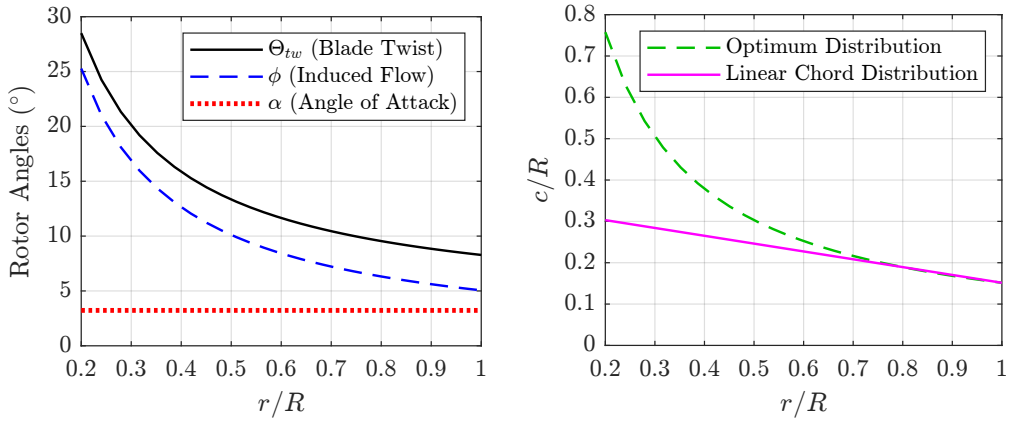

(a) (b)

Figure 2. Nominal geometry and performance of optimum hovering rotor: (a) twist, induced flow, and angles of attack and (b) chord distributions (nominal and simplified linear taper).

optimum distribution from $0.75 \leq r/R \leq 1.0$. Because this is the region of the blade that is associated with the majority of thrust generation, it is believed to be an appropriate simplification.

Table 1 contains the pertinent geometric and operating design conditions of the rotor. These design parameters were defined based on the assumption of a blade composed of a constant symmetric airfoil profile along the blade span. Additionally, a constant zero-lift angle of attack of $\alpha_0 = 0°$ and lift curve slope of $C_{l,\alpha} = 5.7$ 1/rad were employed.

Table 1. Design parameters for the tested propeller.

	Parameter	Value
Geometry	c_{tip}, in. (mm)	0.75 (19.05)
	R, in. (mm)	4.95 (125.73)
	N_b	4
	Airfoil	NACA 0012
	Linear Taper Ratio	2.5:1
Operating Condition	$C_{T_{\text{design}}}$	0.015
	M_{tip}	0.300
	Ω_c (RPM)	7750
	α_{design} (°)	3.25

The propeller blades were 3D printed out of PA 12, 25% mineral-filled nylon via selective laser sintering (SLS) [9]. This material was chosen because of its high stiffness and resistance to moisture absorption. One artifact of printed parts using this material is the considerable resulting surface roughness of the part. This is illustrated in the close-up photograph of one of the fabricated propeller blades in Fig. 3. While smoothing of the blade surfaces was considered (such as via sanding), this was decided against in an effort to simulate a fully turbulent flow over the blade.

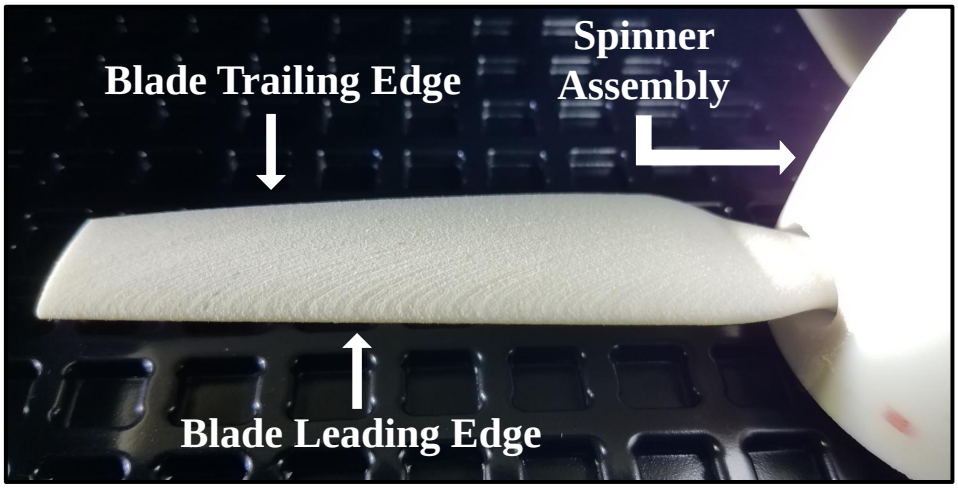

Figure 3. Close-up view of fabricated propeller blade illustrating blade surface roughness.

In other words, the surface roughness of the fabricated blade was used as an artificial boundary layer "trip" to simulate higher Reynolds number flow. As is discussed in Section 4.1, this assumption was met with mixed results in terms of the lift (thrust) and drag (torque) performance of the propeller blades.

2.1.2 Duct Design

Previous researchers have shown that the design of a duct can have a significant impact on both the aerodynamic and acoustic characteristics of the propulsor. For example, a poorly shaped duct can induce flow separation from the inlet, which reduces the aerodynamic performance and increases noise [10, 11]. The goal of this study was to characterize a "good" duct design with reasonable aerodynamic and acoustic characteristics. More specifically, the design was based on rules of thumb from previous aerodynamic studies [5, 10, 12]. Because the guidelines often depend on operating conditions, it is useful to note that this study is focused on static and low speed axial inflow.

The inner diameter of the duct was selected to be 10 inches to match previous tests [10, 11, 13–15]. While the small size could limit the applicability of the results to larger passenger carrying vehicles, Grunwald and Goodson [3] concluded that small-scale models can be used to approximate full-scale performance if duct-lip separation is avoided. Black and Wainauski [16] noted that lip shape is the single most important design parameter affecting separation, particularly at static conditions. They found that a lip defined as:

$$y = \frac{t}{3}\left(\pm 0.2065 * \sqrt{52.75 - \left(3.75 - \frac{3x}{t}\right)^3} + \frac{1}{3}\left(3.75 - \frac{3x}{t}\right)^3 * .028457 + 1.5\right)$$
$$\text{for } \; x < 0.2c \tag{5}$$

avoided flow separation at static conditions on a 30 inch inner diameter duct. In this context, c is the duct chord, t is the maximum duct thickness, and x is the axial or chordwise dimension. Lip shape, however, is not the only important parameter. Black and Wainauski also noted that duct thickness (at the propeller plane) should be at least 10% of the propeller diameter to avoid separation at static conditions. With that guidance in mind, the duct tested in this study had a lip shape matching Eq. 5 with a maximum thickness of 1.2 inches.

The duct area ratio, defined as duct exit area divided by the propeller disk area, is an important design parameter affecting the aerodynamic performance of the duct. A value of 1.15 was selected for this study to match the design of Whiteside et al. [2]. An area ratio greater than one implies an area expansion. A gradual expansion is preferred to avoid diffuser separation and achieve good aerodynamic performance. To maintain a moderate diffuser angle, the duct chord was selected to be 6.67 inches. Table 2 summarizes the key duct design parameters.

Table 2. Design parameters for propeller duct.

Parameter	Value/Basis
Inner Diameter, in. (mm)	10.00 (254.0)
Chord Length, in. (mm)	6.67 (169.4)
Maximum Thickness, in. (mm)	1.20 (30.5)
Area Ratio	1.15
Lip Section	Eq. 5, Ref. [16]
Diffuser Section	NACA 0018

The inner surface of the duct from 20% to 50% of the chord is cylindrical – or straight – with a diameter of 10 inches. The diffuser, which goes from 50% of the chord of the duct cross section to the trailing edge of the duct was designed by scaling a NACA 0018 airfoil. On the exterior surface of the duct, the straight cylindrical portion extends from 20 to 30% of the chord and the last 70% of the chord is shaped to match a NACA 0018 airfoil. For manufacturing reasons, the duct trailing edge was rounded with a radius is 0.05 inches. The final duct cross section shape is shown in Fig. 4. Note that the duct is axisymmetric, aside from a mounting adapter built into the exterior surface, as depicted in Fig. 5.

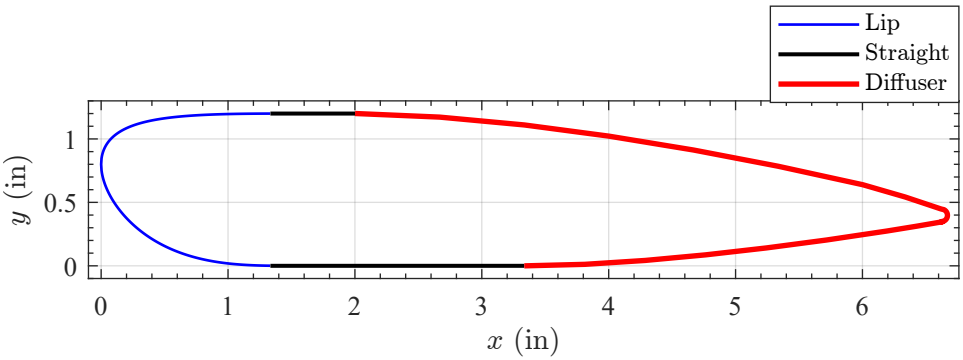

Figure 4. Segments of the tested duct geometry.

The duct was 3D printed from a polycarbonate material (PC-10) using a sterolithog-

raphy process. The walls of the duct are solid (0.060 inches thick) but a partial build density was used in the interior to save material. For both aerodynamic and acoustic purposes, it is desirable to minimize the tip gap between the propeller and duct inner surface. If the tip gap is too small, however, rig misalignment, vibration, or blade elongation could cause the propeller to contact the duct. For this test, the gap between the propeller tip and duct was 0.05 inches.

The axial position of the propeller in the duct can also be important. For this test, the propeller was positioned 3 inches (45% of the duct chord length) behind the duct leading edge. In most previous studies, the propeller was positioned farther forward to increase the separation distance (and therefore reduce interference) with the exit vanes. Since exit vanes were not included in this study, a more symmetric position was selected for the propeller.

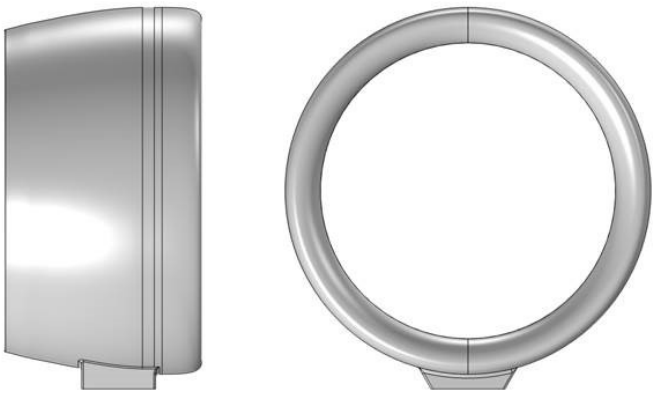

(a) Side view (b) Front view

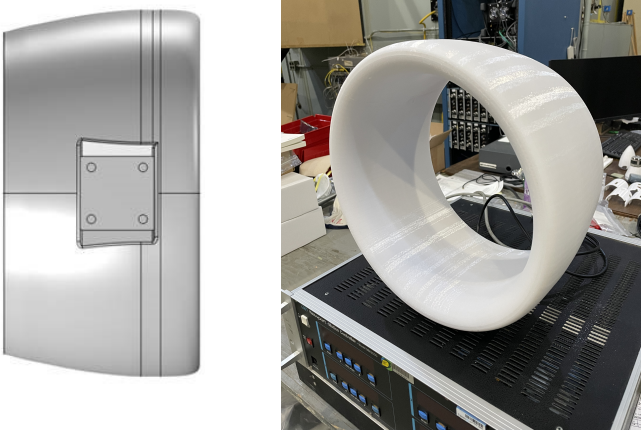

(c) Bottom view (d) Photograph

Figure 5. Visualizations and photograph of complete, three-dimensional duct geometry.

2.2 Testing Facility and Instrumentation

Tests were conducted in the NASA Langley Small Hover Anechoic Chamber (SHAC) [17], formerly known as the Small Anechoic Jet Facility (SAJF) [18]. SHAC is an acoustically treated facility with a cut-on frequency of 250 Hz and measures 3.87 m $\times$ 2.56 m $\times$ 3.26 m (L $\times$ W $\times$ H) from wedge tip to wedge tip. It has an air inlet and outlet, through which a freestream flow of approximately 5 m/s is possible with the use of a downstream single speed fan. This freestream flow was originally intended to serve as a freestream co-flow for scaled jet nozzle experiments. In the current study, this freestream flow is utilized to provide initial insight into ducted rotor performance under a slight non-zero inflow condition. It is important to note that the flow conditioning is only comprised of a 6 inch (152 mm) deep honeycomb filter installed within the SHAC inlet nozzle. The freestream turbulence intensity at the core flow centerline was measured to be rather large at $TI = 100 \times U_{\text{rms}}/U_{\infty} \approx 4.2\%$ at the approximate test article location.

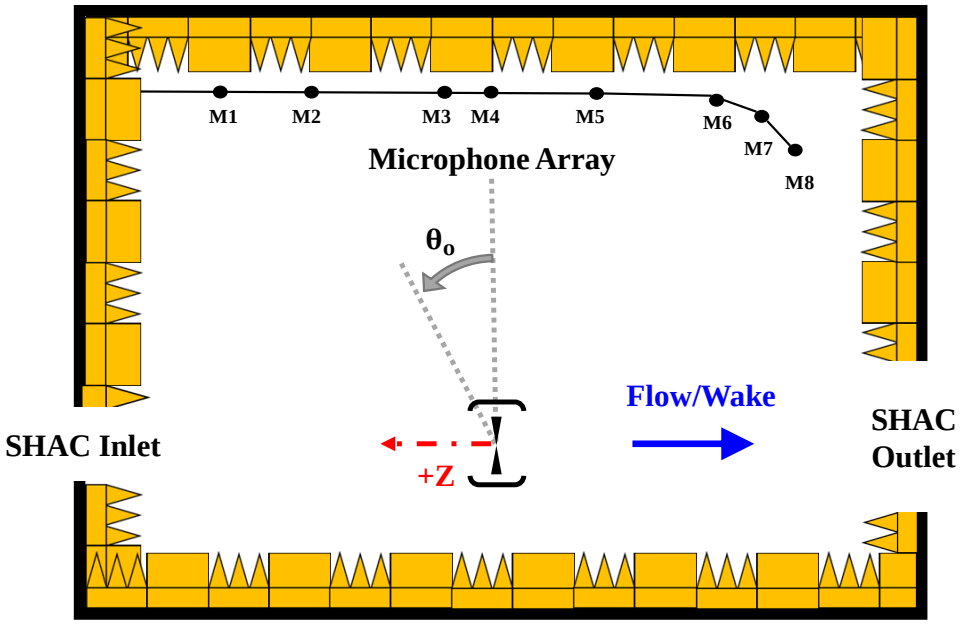

Figure 6. Illustration of SHAC facility detailing propeller thrust direction (+Z), microphone angle convention (θ_o), and flow direction. *Note: not drawn to scale.*

As shown in Fig. 6, the SHAC contains an eight element microphone array that encompasses a range of directivity angles. The sensors are 6.35 mm-diameter free-field Brüel & Kjær microphones with associated preamplifiers. The microphones are powered using the facility data acquisition system (discussed in Section 2.4) and are operated for all testing conditions with the protective grid caps removed. This allows for a nearly flat free-field frequency response up to approximately 80 kHz. Their locations in terms of a radial distance and elevation angle relative to the propeller hub center are provided in Table 3.

Several photographs of the facility are provided in Fig. 7 for the tested isolated propeller configuration. The propeller hub assembly is positioned at the middle of

Table 3. Microphone locations relative to propeller hub.

Microphone #	Radial Distance (m)	θ_o (deg.)
1	2.38	37.3
2	2.10	25.8
3	1.94	5.7
4	1.91	-0.8
5	2.04	-19.2
6	2.30	-35.2
7	2.31	-43.5
8	2.23	-50.1

the facility in the lengthwise (axial) direction, approximately coinciding with the axial location of the middle element of the microphone array (microphone 4). The rotor stand that supports the test articles is comprised of slotted Aluminum square channels with a 90 degree junction, from which extends a hollow steel cylindrical conduit. Test articles are then mounted to the end of this conduit via an adapter plate.

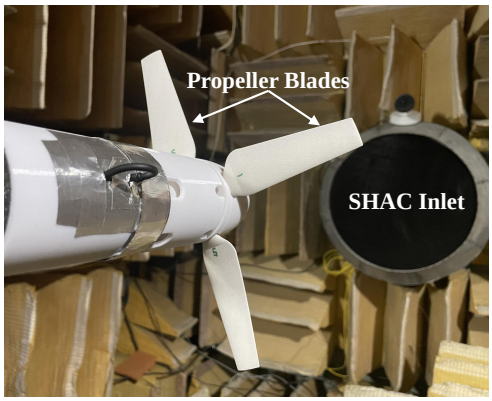

(a) Upstream view

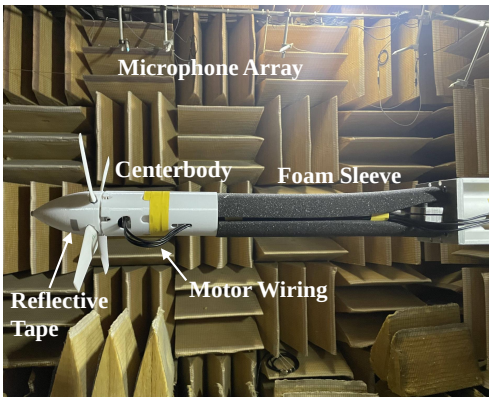

(b) Sideline view

(c) Downstream view

Figure 7. Photographs of the SHAC facility with isolated propeller hardware installed.

Two load cells were utilized in this testing campaign: one for measuring propeller thrust and torque, and one for measuring duct thrust/drag. Both of the load cells used in this study were ATI-IA Mini40 multiaxis load cells, which have six degree-of-freedom measurement capabilities. The locations of the respective propeller and duct load cells are depicted pictorially in Fig. 8. As is shown in Fig. 8(a), the

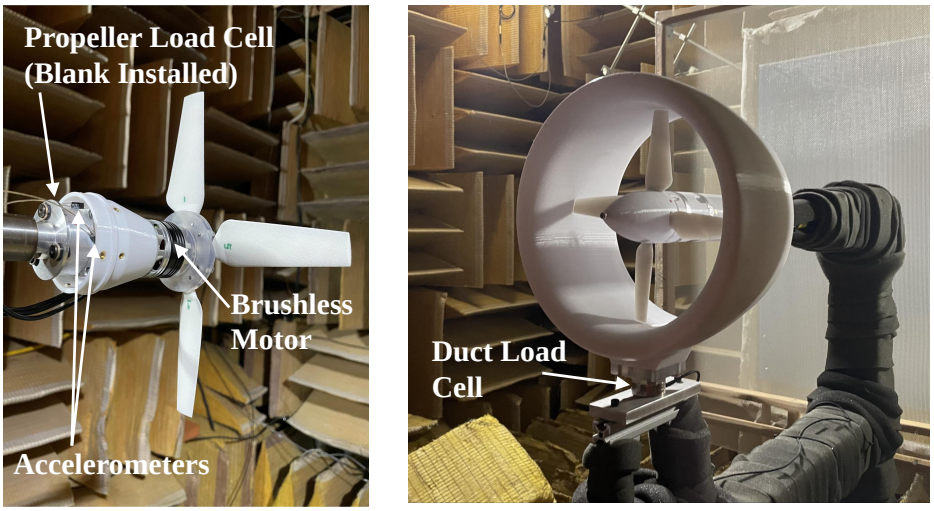

(a) Propeller assembly (b) Duct

Figure 8. Photographs of near-field instrumentation on SHAC test articles.

propeller load cell is oriented such that the thrust is measured in the direction normal to the load cell mounting surface (+Z direction). Meanwhile, Fig. 8(b) shows that the duct load cell is mounted in an upright orientation at the base of the duct such that the axial force (thrust or drag) of the duct is measured parallel to the load cell measurement face (+X direction). Also shown in Fig. 8(a) are two single-axis accelerometers that were utilized in the early phases of testing to quantify lateral displacements of the propeller hardware under the range of tested conditions. This was important because it verified that the deflections of the apparatus under operation were very small such that the propeller blades would not physically contact the inner surface of the duct. Note that no accelerometer data is presented in this report. Finally, the propeller system was powered using a KDE Direct 3510XF brushless motor, which was affixed to the measurement side of the load cell via a conical plastic insulator piece. The motor, insulator, and propeller load cell assembly were then shrouded by plastic cylindrical shell pieces to represent the propeller centerbody. Note that the centerbody pieces are outfitted with a series of cutouts to allow for air ventilation and cooling of the brushless motor.

The rotation period of the motor-propeller assembly was measured using a non-intrusive Remote Optical Laser Sensor (ROLS) and ACT-3X tachometer panel manufactured by Monarch Instrument. The tachometer provided a Transistor-Transistor Logic (TTL) pulse each time the output laser beam encountered a piece of reflective tape (see Fig. 7(b)) that was positioned on the rotating assembly.

2.3 Test Conditions

Near-field aerodynamic loads and far-field acoustic measurements were acquired on the isolated and ducted propeller configurations across a range of propeller rotation rates. It is worth noting that while the propeller hub used in this study allows for adjustability of the propeller pitch (or collective setting), it was monitored and kept constant for this entire investigation. Specifically, this collective setting was enforced with the use of a propeller pitch gauge at the tip of the propeller, where the angle measurement was set to $\Theta_{\text{tip}} \approx 8.0°$. This corresponds to the nominal setting based on the optimum hovering rotor design parameters discussed in Section 2.1.1.

Both open and ducted propeller configurations were tested in static hover and low speed forward flight ($U_\infty \approx 5.2$ m/s) over a propeller tip speed range of $0.12 \leq M_{\text{tip}} \leq 0.32$. Testing static hover conditions required the installation of two screen meshes of different percentage open area downstream of the rotor stand [19]. The purpose of these screens is to delay the onset of flow recirculation by breaking up the wake structures of highest energy shed by the propulsor and reducing the energy of the recirculated flow. This is important because this flow recirculation can dramatically alter the acoustic content of a rotor system [20]. Figure 9 provides images of the dual screen mesh treatments installed for static hover measurements of both open and ducted propeller configurations. It is also worth noting, via Fig. 9, that the

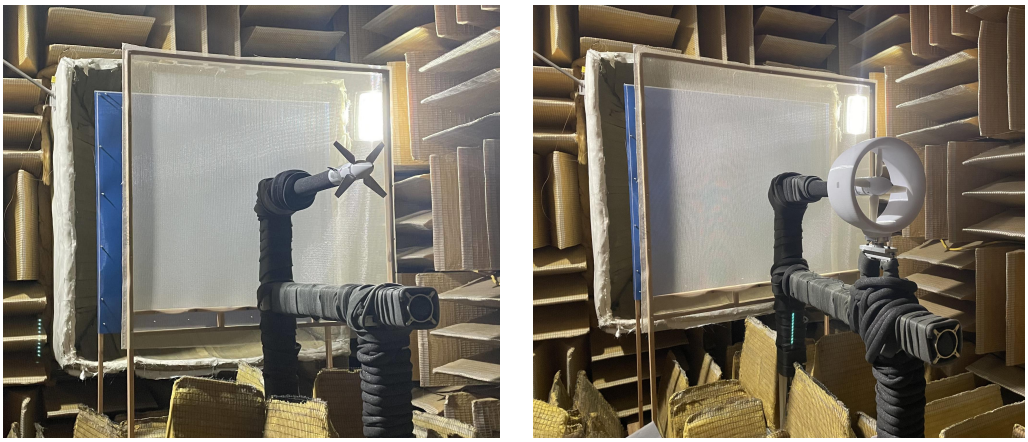

(a) Open propeller (b) Ducted propeller

Figure 9. Photographs of complete open and ducted propeller assemblies with facility in static hover mode.

horizontal channel onto which the duct support structure was installed, remained present for all testing conditions and configurations. While this did potentially represent an acoustically reflective structure, the authors deemed it appropriate to leave in place so as not to introduce facility differences other than those related to the duct itself. It is believed that relative acoustic comparisons can still be made between the open and ducted propeller data sets.

2.4 Data Acquisition and Post-Processing

Dynamic propeller rotation rate, aerodynamic loading, and acoustic data were acquired using a Brüel & Kjær LAN-XI data acquisition system coupled with the BKConnect software package. All data were acquired at a sample rate of 131,072 Samples/s, and the anti-aliasing filter of the LAN-XI system yielded a flatband spectrum measurement up to 51.2 kHz. Data acquisition runs were approximately ten seconds in duration. Static hover runs consisted of a rapid ramp-up of the propeller assembly rotation rate to a desired steady state target operating condition. The ramp-up period lasted approximately two seconds. The remaining eight seconds was comprised of a "clean" propeller operation condition, followed by a "dirty" operation condition characterized by an onset of flow recirculation in the facility. The time duration of clean operation varied based on the desired rotation rate condition, and thus thrust generation by the propeller. Low speed forward flight runs, meanwhile, were able to be run more continuously from one test point to the next because the only parameter that needed to be changed was the propeller rotation rate. It is worth noting that the mesh screens depicted in Fig. 9 were not installed for these conditions.

A useful acoustic processing tool for rotor systems is periodic and broadband differentiation. This allows for the discernment of noise contributions by the system that are deterministic (frequencies that have constant phase and are harmonics of the fundamental system rotation rate), and those that are residual or stochastic in nature (random in phase). The former of these acoustic sources are better known as the steady thickness and loading sources of rotating blade noise [21], while the latter are non-deterministic and typically the result of turbulent flow interactions on or near the rotating blade surface [22].

Periodic and broadband extraction is performed in this study by discretizing the measured acoustic pressure time histories into data blocks corresponding to the rotor period of revolution, computing an average revolution acoustic time history, then repeating this averaged time history and subtracting it from the raw measured signal. More details of this procedure are provided in Ref. [23]. An illustration of the periodic and broadband noise extraction processing methods applied to SHAC microphone 6 for a propeller tip Mach number of $M_{\text{tip}} = 0.30$ is provided in Fig. 10.

As can be seen in Fig. 10, extraction of a residual spectrum still contains remnant tonal features. These remnant tones are not removed in the periodic extraction because of two primary physical causes: (1) the tonal noise is caused by the motor and slight variations in rotation rate make these tones difficult to completely remove, or (2) the remnant tones have a random phase that is not directly related to the steady rotational noise generated by the propeller system. The first of these remnant noise features tends to occur at rather high frequencies, where rotation speed variations make the periodic extraction process more difficult. The second of these sources, however, is related to turbulence ingestion into the propeller disk. The source of this turbulence is usually eddies that are introduced by the inlet of the facility and/or due to the interaction of the propeller blades with the wake of the preceding blade. Both of these sources are evident in the data presented in this report and occur across different frequency ranges, which are discussed in Section 4.2. An additional

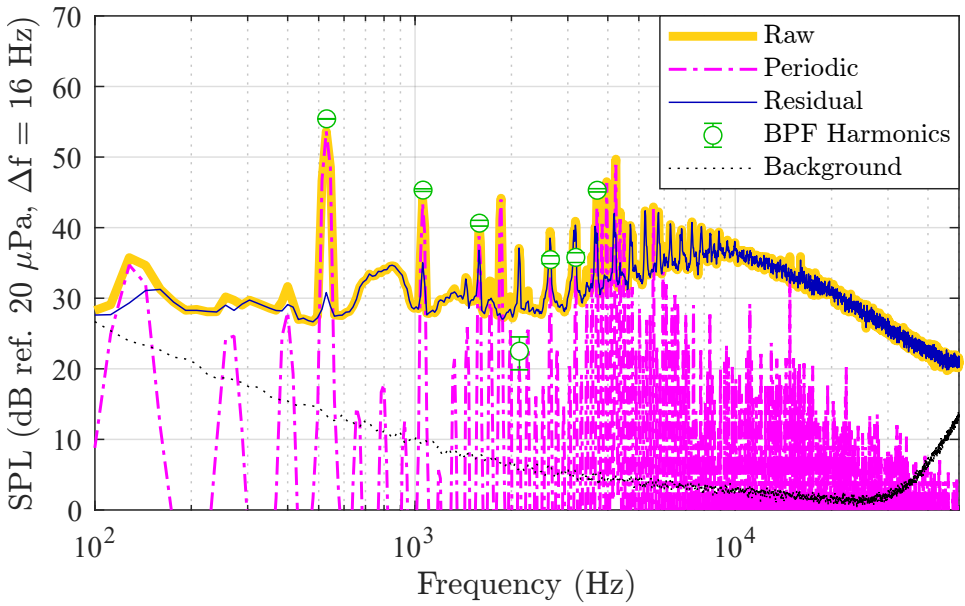

Figure 10. Narrowband acoustic spectra of the isolated propeller in static hover at $\theta_o = -35°$ (microphone 6) illustrating acoustic post-processing methods. Propeller operating condition of $\Omega = 7943$ RPM ($M_{\text{tip}} = 0.30$).

post-processing method that is applied to the extracted residual spectra data is the removal of remnant tones, which is visually demonstrated in Fig. 11. The purpose of this final processing step is to omit the spectral artifacts that are believed to be related to interaction of turbulent structures with the propeller blades (such as those that can result from perpendicular blade vortex interactions [24]).

As Figs. 11(a) and 11(b) show, periodic extraction removes the majority of the highest-amplitude tones, which indicates that they have a strong, consistent phase relationship with the rotation frequency of the propeller system. However, as Fig. 11(b) shows, a non-negligible amount of tonal peaks remain. These tones manifest in the form of integer multiples of the fundamental BPF of the propeller between 3 and 15 harmonics (or between 1 and 6 kHz). These are believed to be related to turbulence and/or blade wake ingestion. Furthermore, there is a cluster of high-frequency tones also visible between 15 and 19 kHz. These are believed to be due to the pulse width modulation (PWM) rate of the brushless motor and electronic speed controller (ESC) system. This tonal cluster was found to remain approximately consistent, regardless of the rotation rate of the propeller. Finally, the remnant peaks are removed with the application of a spectrum amplitude smoother in which the peaks are identified and averaged out using the acoustic levels of the neighboring frequency bins. The results of applying this spectrum smoother are shown in Fig. 11(c). More details on this final processing step are provided in Ref. 25.

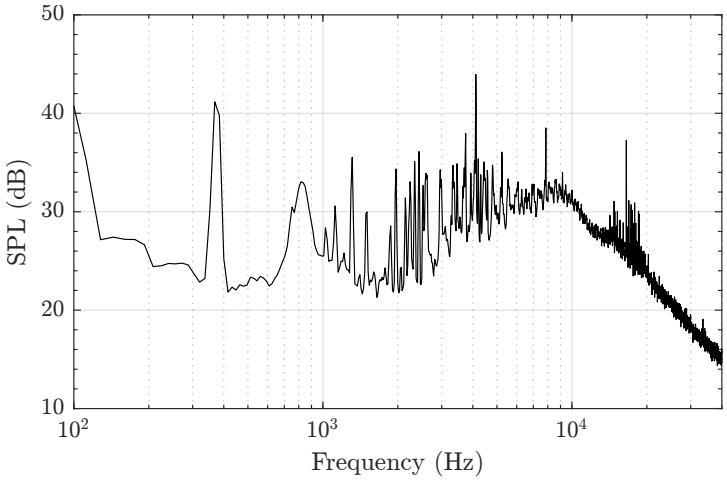

(a) Raw

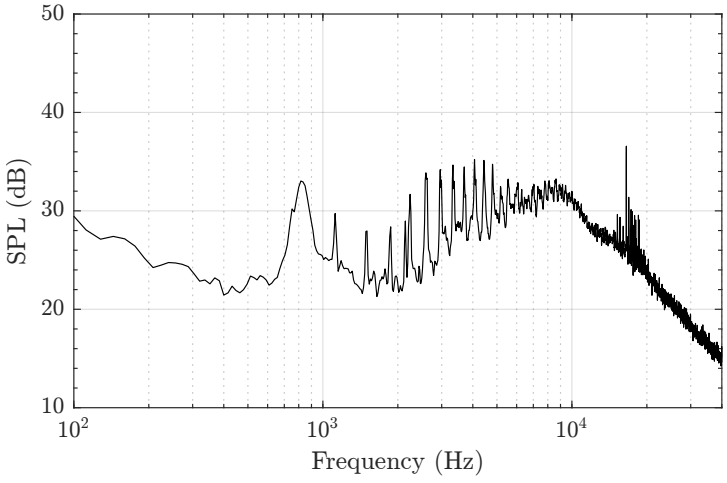

(b) Residual

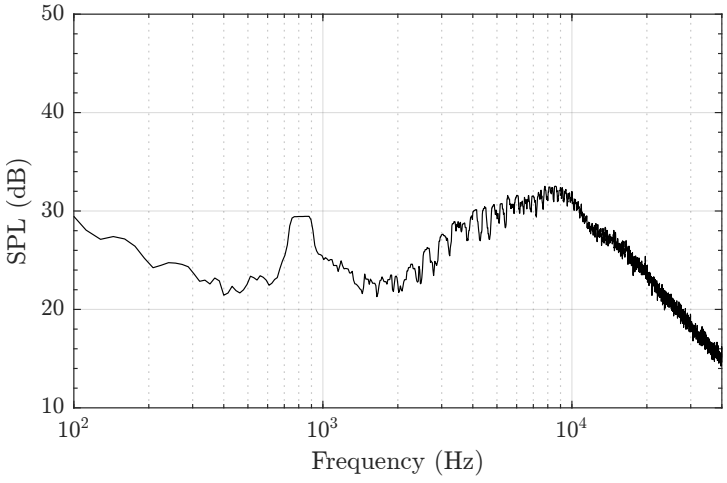

(c) Tone-removed Residual

Figure 11. Illustration of periodic extraction and remnant tone removal processes. Data shown is for $\theta_o = -35°$ (microphone 6) of the isolated propeller operating at $\Omega = 5613$ RPM ($M_{\text{tip}} = 0.214$) in hover.

3 Modeling Approach

Three low-fidelity modeling tools were utilized in this study to characterize the performance of the isolated and ducted propeller configurations. For the isolated propeller configuration, the Propeller Analysis System portion of the NASA Aircraft NOise Prediction Program (ANOPP-PAS) [26] was leveraged. As the name of the software suite implies, the noise of the propeller system is also possible to predict. It is important to note, however, that only the tonal or deterministic components of noise can be predicted by this software. Furthermore, the aerodynamic performance of the ducted propeller configuration is assessed using simple momentum theory [8] and the Ducted Fan Design Code (DFDC), [27] which is a coupled lifting-line and vortex lattice panel method that respectively represent the rotor/propeller and duct/centerbody components of the system.

3.1 Isolated Propeller Modeling

ANOPP-PAS (herein referred to as PAS) utilizes blade element momentum theory (BEMT) to predict the aerodynamics and noise of subsonic propellers. [26] The blade profile analysis modules of PAS include a coordinate transformation using a Joukowski transformation, potential flow around the blades computed by Theodorsen's method using the Kutta condition to fix circulation, and boundary layer analysis using the Holstein-Bohlen or Truckenbrodt methods for respective laminar and turbulent regions. Propeller performance and induced flow are then computed using Lock's method with the Prandtl circulation function for the blade tip region. Finally, a Subsonic Propeller Noise (SPN) module is utilized for computing deterministic acoustic pressure time histories and spectra at defined observer locations. This noise module is a direct implementation of Farassat's F1A FW-H acoustic solver. [28, 29]

It is important to note that PAS is designed to model propellers in forward flight and not rotors in hover conditions. In other words, PAS cannot compute the aerodynamic performance and thus acoustics of a spinning blade in the absence of a freestream velocity condition. Therefore, a constant forward flight speed corresponding to the low-speed axial flow condition of SHAC is implemented for all simulated operating conditions. The hovering conditions are simply simulated by adjusting the collective of the propeller blades such that their predicted torque generation matches that measured in the experiment. While thrust is the typical tuning aerodynamic parameter, it was found that thrust-matching between experiment and prediction would result in more than a 10% deficit in predicted torque. This deficit is likely due to the coarse texture of the tested blades, which results in considerably higher levels of blade drag than would otherwise be generated by blades with a smooth surface. An illustrative comparison between a PAS acoustic prediction and SHAC measurement is provided in Fig. 12. As this figure shows, the PAS-predicted propeller BPF acoustic levels are comprised of thickness and loading noise contributions, the summation of which yields the total SPL. The comparison is fairly good, with the largest discrepancy of approximately 5 dB occurring at $\theta_o = 37.3°$ (microphone 1). All other experimental microphone measurements are within 2.5

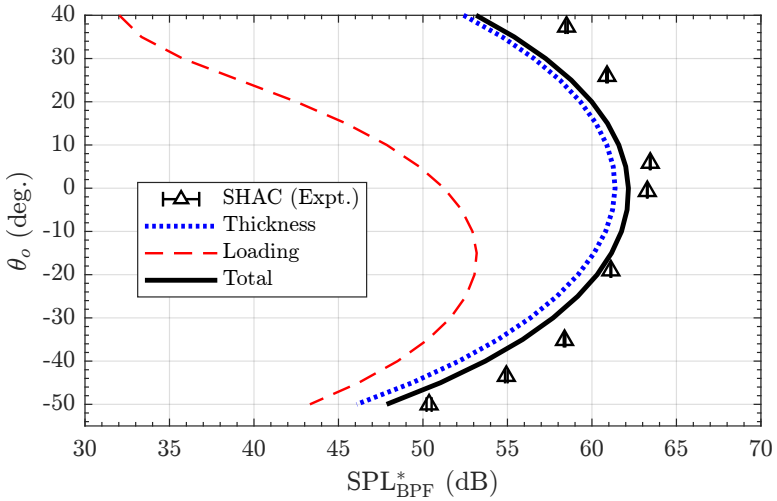

Figure 12. BPF SPL directivity comparison between SHAC experimental measurements and predictions using ANOPP-PAS. *Isolated propeller in hover at* $M_{\mathrm{tip}} = 0.315$.

dB of the PAS prediction. Another important takeaway from this plot is that the BPF acoustic amplitude is largely dominated by the steady thickness component of noise. This means that the majority of the noise generated at this frequency is due to the propeller blade motion, rather than due to the aerodynamic loads generated by the blades. This has important implications when comparing acoustic amplitudes between the isolated and ducted propeller configurations, which is done in Section 4.2.

3.2 Ducted Propeller Modeling

3.2.1 Momentum Theory

In an effort to model the thrust contributions of the ducted propeller system in this study, simple momentum theory can be applied to the case of a non-ideal hovering ducted rotor [8]. Figure 13 provides a schematic illustrating the pertinent parameters in the momentum theory analysis for a ducted rotor in hover. Rather simply, conservation of mass for subsonic flow between the rotor plane and a plane downstream of the duct (3) yields the following:

$$\dot{m} = \rho A_R v_i = \rho A_3 w, \tag{6}$$

where $\dot{m}$ is the mass flow rate of air through the duct, ρ is the ambient and freestream air density (assumed to remain constant), v_i is the velocity induced by the rotor, A_R is the area of the rotor disk, and A_3 is the area of the wake below the rotor, which is larger than A_R. The area ratio between the wake station and rotor disk can therefore be expressed as

$$a = \frac{A_3}{A_R} = \frac{v_i}{w} \tag{7}$$

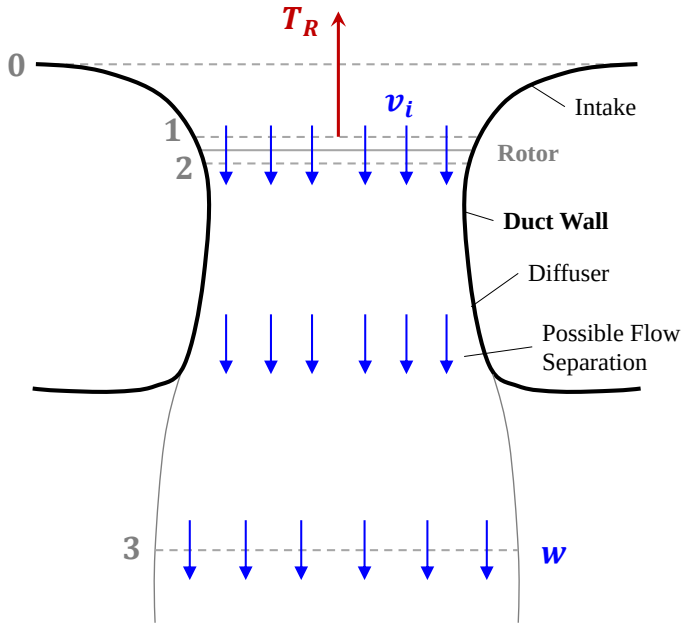

Figure 13. Schematic of momentum theory model applied to a non-ideal ducted rotor in hover. *Illustration adapted from Reference 8.*

Conservation of momentum can then be utilized between stations (0) and (3), where air molecules transition initially from zero velocity to a velocity of w in the wake. This can be stated in terms of the total thrust generated by the system as

$$T_{\text{Total}} = T_D + T_R = \dot{m}w. \tag{8}$$

Incorporating Eqs. 6 and 7 into Eq. 8 therefore yields

$$T_{\text{Total}} = \frac{\rho v_i^2 A_R}{a} \tag{9}$$

Bernoulli's equation is applied to the area between the duct intake station (0) and the upstream rotor station (1):

$$p_0 = p_1 + \frac{1}{2}\rho v_i^2. \tag{10}$$

It is worth noting that location of station (0) does not necessarily coincide with the leading edge of the duct intake, but rather, is intended to represent a location far enough upstream where a static ambient condition can be realized. Next, Bernoulli's equation can be applied between the station immediately downstream of the rotor plane (2) and the duct flow outlet area (3):

$$p_2 + \frac{1}{2}\rho v_i^2 = p_0 + \frac{1}{2}\rho w^2, \tag{11}$$

where w is wake velocity downstream of the duct. Furthermore, the thrust generated by the rotor, T_R, can be solved for by substituting Eq. 10 for the freestream pressure

p_0 in Eq. 11 to yield

$$T_R = (p_2 - p_1)\, A_R = \frac{1}{2}\rho w^2 A_R. \tag{12}$$

Now, the contribution of the thrust generated by the rotor to the total thrust generated by the ducted rotor system can be found by dividing Eq. 12 by Eq. 9:

$$\frac{T_R}{T_{\text{Total}}} = \frac{1}{2}\frac{\rho w^2 A_R a}{\rho v_i^2 A_R}. \tag{13}$$

This expression can be simplified by substituting $v_i = aw$ from Eq. 7 to yield

$$\frac{T_R}{T_{\text{Total}}} = \frac{1}{2a}. \tag{14}$$

In other words, the ratio of thrust generated by the rotor to the total ducted rotor system thrust is the inverse of twice the area ratio.

For the sake of simplicity, the plane of the duct wake (station 3 in Fig. 13) is taken at the physical trailing edge of the duct. This is because the area ratio between this location and the propeller is known to be $a = 1.15$, which was previously reported in Table 2. Therefore, Eqn. 14 yields an ideal rotor thrust contribution of $T_R = 0.44 * T_{\text{Total}}$, or 44% of the total system thrust. Consequently, the duct would generate 56% of the total system thrust. It is important to note, however, that this assumes that the flow through the duct remains attached all the way to the duct trailing edge. In reality, some portion of flow separation along the duct wall is likely to occur, considering that the duct design is not optimized. This flow separation would effectively reduce the "effective" exit area of the duct, which would in turn reduce the value of the area ratio. However, as will be seen in Section 4.1, this estimate based on simple momentum theory offers a good initial approximation.

3.2.2 Ducted Fan Design Code

The DFDC represents an extension of the XROTOR propeller design code, with a more detailed treatment of the effects of a duct and propeller centerbody. Specifically, it allows for the prediction of the mean aerodynamic loads and flowfield of a ducted propulsor with relatively large induced velocities relative to a freestream velocity, which is applicable to hover operating conditions. DFDC also models the viscous loss effects and non-uniform loading effects in the calculation of the duct flowfield. [27]

An example of the ducted propeller case setup in DFDC is provided in Fig. 14. This figure details both the discretized flowfield as well as the individual solid bodies in the simulation as: (1) propeller centerbody, (2) duct shroud, and (3) propeller blades. The case was setup using the default propeller blade airfoil aerodynamic parameters, which was believed to be suitable for a first-round of simulations based on the constant NACA 0012 airfoil cross-sections that make up the propeller blades. This was expected, however, to yield an overprediction in propeller thrust and underprediction in torque due to the very coarse texture of the fabricated propeller blades. In other words, the blade texture was expected to reduce the lift and increase the drag behaviors of the propeller blades, respectively.

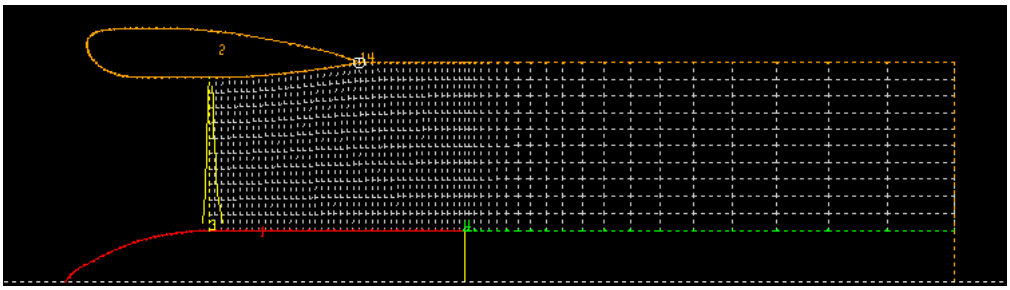

Figure 14. DFDC case setup for current ducted propeller configuration. *Note: Flow is from left to right.*

4 Results and Discussion

In this section, the aerodynamic and acoustic experimental results will be presented on both isolated and ducted propeller configurations for simulated hover and low speed axial forward flight conditions. The aerodynamic results of the ducted propeller will also be complemented by predictions using the DFDC code, while both aerodynamic and acoustic results of the isolated propeller will be complemented by predictions using the ANOPP-PAS [26] and ANOPP-ROTONET [30] codes. While comparisons are made in the following section between the isolated and ducted propeller configurations, it is important for the reader to keep in mind that it is difficult to directly relate the two, due to their vastly different geometries. Therefore, the purpose of the comparisons is not to necessarily promote one configuration over the other, but rather to identify the differences and provide possible physical explanations.

4.1 Aerodynamics

The pertinent aerodynamic behaviors of the isolated and ducted propeller configurations are discussed in the following sections under hover and low-speed axial forward flight conditions. While these operating conditions tend to be differentiated conventionally using rotor and propeller nomenclature, common rotor nomenclature is utilized for all measured operating conditions. Both dimensional and nondimensional aerodynamic loads are considered. Dimensional loads are presented relative to sea-level standard day (SLSD) conditions, the definitions of which are provided in Ref. 23. Nondimensional loads are presented in the form of the thrust coefficient (C_T) and the power coefficient (C_P). These are respectively defined as

$$C_T = \frac{T}{\rho_\infty A \Omega^2 R^2}, \tag{15}$$

and

$$C_P = \frac{P}{\rho_\infty A \Omega^3 R^3}, \tag{16}$$

where $A = \pi \left(R^2 - r_{\text{cb}}^2\right)$ is the propulsor disk area based on the propulsor and centerbody radii, respectively, T is the dimensional thrust measured by the propeller and/or duct load cells, and the dimensional power $P = Q\Omega$, where Q is the measured torque generated by the propeller. These definitions are maintained across both physical propulsor configurations as well as flow conditions, the primary difference being that the propeller disk area is based on the propeller tip radius ($R = 125.73$ mm), while the duct disk area is based on the radius of the duct inner wall ($R = 127$ mm).

Estimates of aerodynamic efficiency are provided in the following sections using conventional rotor and propeller definitions for respective hover and axial inflow conditions. For simulated hover conditions, this is defined using power loading, which is simply defined as

$$\text{PL} = \frac{T^*}{P^*}, \tag{17}$$

where T^* and P^* are the SLSD-corrected net thrust and mechanical power of the propulsor. For low-speed axial inflow conditions, the conventional propulsive efficiency is used in the form

$$\eta = \frac{TU_\infty}{P}, \tag{18}$$

where the freestream velocity in SHAC was previously measured to be $U_\infty \approx 5$ m/s. Also applicable to the cases of low-speed axial inflow is the advance ratio:

$$J = \frac{U_\infty}{nD_p} = \frac{M_\infty \pi}{M_{\text{tip}}}. \tag{19}$$

4.1.1 Hover Performance

Figure 15 provides measured profiles of dimensional and nondimensional thrust and power with respect to tip Mach number for isolated and ducted propeller configurations at simulated hover conditions. The data in this figure are provided with error bars that represent the worst-case amount of drift in the load cell measurement for

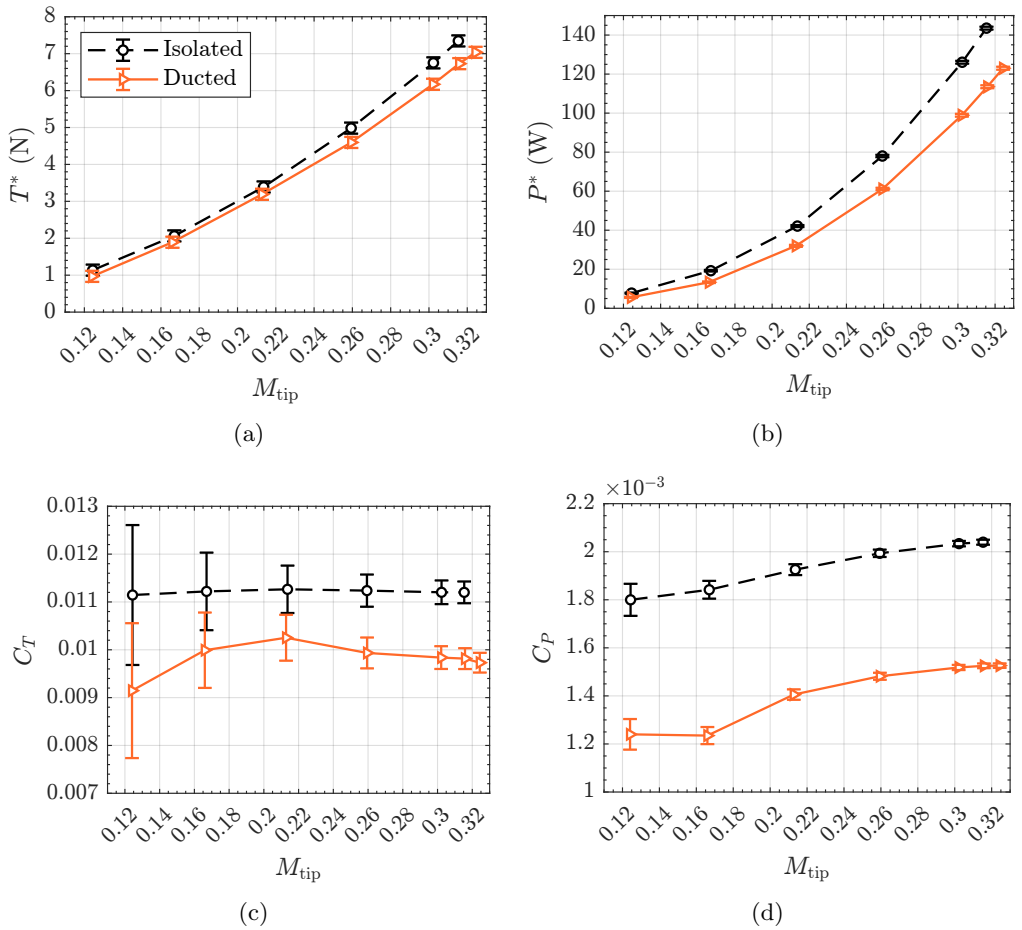

Figure 15. Measured thrust and power variations with tip Mach number for isolated and ducted propeller configurations in simulated hover conditions.

the testing sequence. These dimensional uncertainty values present themselves as constant error values for the dimensional load plots in Figs. 15(a) and 15(b), and as decreasing error values with increasing M_{tip} in Figs. 15(c) and 15(d). This decrease in error with increasing tip speed is due to the constant dimensional uncertainty value being divided by an increasing tip velocity value as indicated in Eqs. 15 and 16. It is worth noting that the thrust data for the ducted propeller configuration in Figs. 15(a) and 15(c) are due to addition of thrust contributions by both the propeller and duct components. These individual contributions are detailed later in this section.

Figures 15(a) and 15(b) display second order variations of thrust and power as a function of tip Mach number, which is typical for rotating blade systems. In general, the isolated propeller generates more thrust but requires more power for a given rotation rate condition as compared to the ducted propeller. Furthermore, data of Fig. 15(c) reveals a nearly constant thrust coefficient as a function of tip Mach number for the isolated propeller. This is expected behavior for an optimum hovering rotor because its design is based on a target thrust coefficient condition, its performance of which is not assumed to vary with rotation rate. However, small-scale test articles such as those utilized in this study have a tendency to challenge this assumption, either due to physical measurement limitations on parameters such as blade shape and collective, and/or due to low Reynolds number effects. Therefore, the constant C_T behavior shown in Fig. 15(c) resembles that of a blade at higher Reynolds numbers, possibly due to the coarse texture of the printed blades that can "trip" the boundary layers and force a fully turbulent condition. Meanwhile, the results for the ducted propeller in this figure show a slight deviation in this trend. Instead, a slight increase in C_T is observed across low tip speeds up to $M_{\text{tip}} \approx 0.21$, after which it appears to level off. While the exact cause of this is currently unknown, some speculations are presented later in this section. The results of Fig. 15(d) show slight increases in C_P with increasing M_{tip} for both propulsor configurations.

Figure 16 shows a comparison plot of the measured power loading variation with propulsor disk loading between isolated and ducted propellers. Note that while these quantities are not nondimensional, they are believed to be the best quantities with which to compare the propulsor configurations due to their different geometries. The results show that the ducted propeller system outputs more overall thrust per unit of power draw than the isolated propeller, across the whole range of tested disk loading conditions. While this may be interpreted to mean that the ducted propeller is more "efficient" than the isolated propeller in this simplified single component test setup, the potential for more complex installation effects of a more realistic, vehicle-installed propulsor or series of propulsors would likely introduce uncertainties to this claim. Possible efficiency reductions of a ducted propulsor can include increases in drag associated with pylon or other airframe fairings needed to integrate the propulsor with the airframe, as well as due to the presence of stator blade assemblies located downstream of the propeller/fan blades.

Figure 17 provides a breakdown of the thrust contributions measured by both the propeller and duct for ducted propeller operations at simulated hover conditions. The results show a nearly equal amount of thrust contributed by these two sub-systems, with the duct actually beginning to contribute slightly more than the

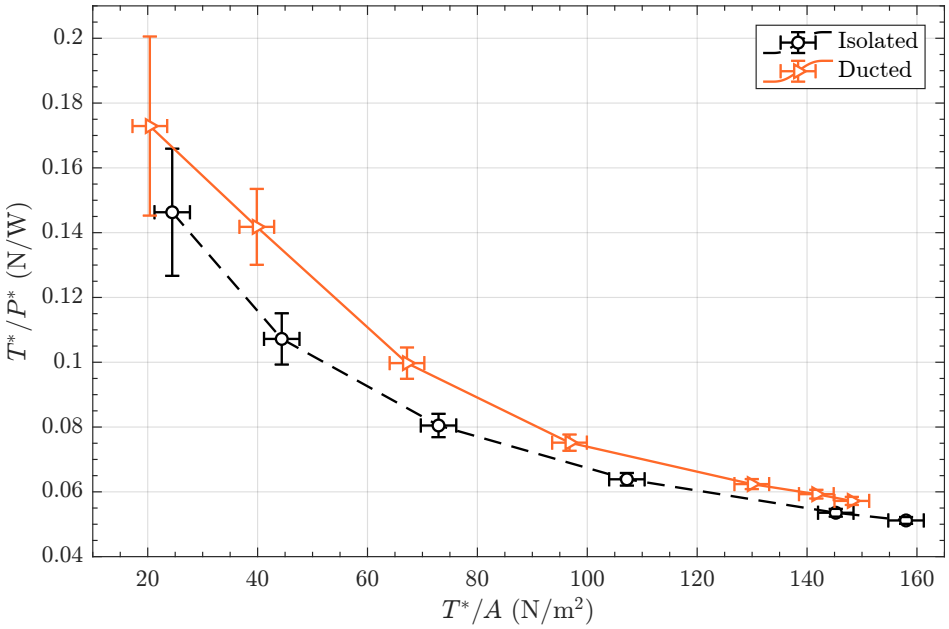

Figure 16. Measured power loading variations with propulsor disk loading for isolated and ducted propeller configurations in simulated hover conditions.

propeller for tip speeds $M_{\text{tip}} \geq 0.30$. It is very likely that the propeller operation at low tip speeds may result in separated flow in the duct leading edge region, which could explain the slightly lower overall C_T values of the ducted propeller at lower tip velocities. Increasing the rotation rate of the propeller likely promotes re-attachment of the flow along the duct wall, which may help explain the asymptotic behavior of C_T and C_P with M_{tip} in Figs. 15(c) and 15(d).

4.1.2 Low-Speed Axial Inflow

Figure 18 provides measured profiles of dimensional and nondimensional thrust and power with respect to advance ratio for isolated and ducted propeller configurations at low-speed axial inflow conditions. These results show an expected decrease in both thrust and power with increasing advance ratio, which is indicative of an increase in freestream velocity relative to the propeller tip speed. It is worth noting that both isolated and ducted propeller configurations exhibit negative thrust (drag) at the highest tested advance ratio condition. It is also worth noting that the ducted propeller system exhibits lower thrust generation and mechanical power relative to the isolated propeller. While this is consistent with the static hover conditions shown in the previous section, the relative decrease in thrust output is considerably greater than the decrease in mechanical power.

The differences in balance of thrust and power between the propulsor configurations is further demonstrated in the propulsive efficiency comparisons shown in Fig. 19. This figure shows that the ducted propeller configuration performs much worse than the isolated propeller across the entire range of tested advance ratios. Furthermore, the peak propulsive efficiencies are seen to be quite low for both con-

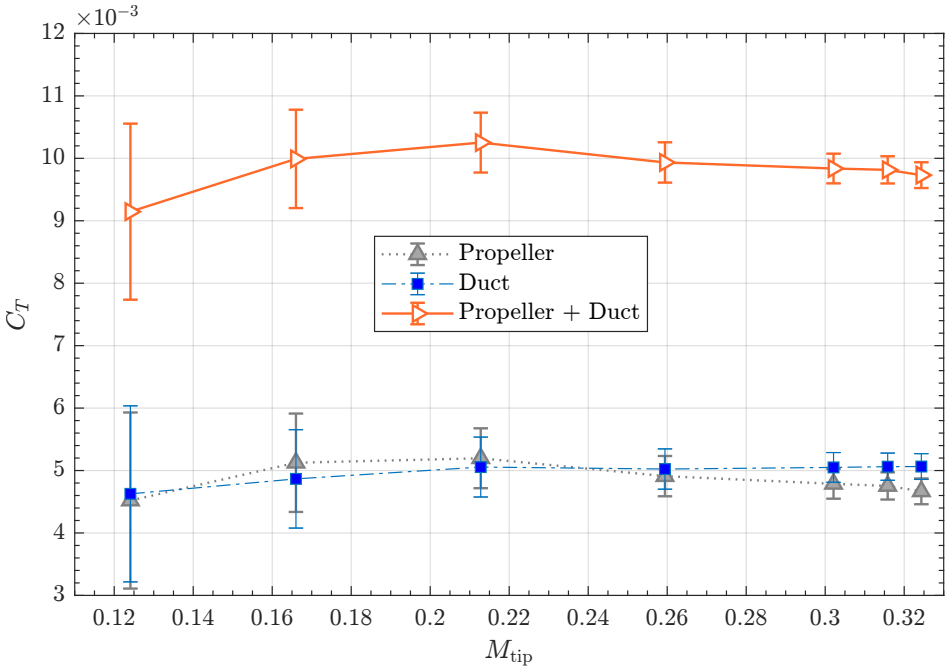

Figure 17. Measured duct and propeller thrust contributions across tested range of tip Mach number conditions in simulated hover conditions.

figurations. This is because of several factors: (1) the propeller was designed for hovering conditions, (2) the pitch of the blades was not changed between either the different inflow conditions or isolated/ducted propulsor configurations, and (3) the torque of the propeller system was considerably higher than that predicted by low-fidelity modeling tools. While items 1 and 2 can be easily explained by changes in angle of attack seen by the blade as a result of either the change in inflow conditions and/or the presence of the duct, item 3 is believed to pertain to the blade fabrication itself.

As was discussed in Section 2.1.1, the propeller blades have a considerable amount of surface roughness that was not quantified. While this is believed to assist in maintaining the constant thrust profile shown previously in Fig. 15(c), it is also believed to be responsible for a considerably higher amount of torque. For example, Fig. 15(d) shows an experimental measurement of $C_P \approx 0.002$ for the target design operating condition of $M_{\text{tip}} = 0.30$. This is in sharp contrast to a ROTONET prediction of $C_P \approx 0.0014$ when thrust-matched to the experimental measurement, which represents a more than 30% underprediction of the measured value. While the surface roughness of the blades is believed to behave effectively as a turbulence "trip", it is also believed to be potentially overtripping the flow over the blade. This in turn results in thicker boundary layers over the blade, which can help explain the higher levels of measured torque. The potential acoustic implications of this are discussed in Section 4.2.

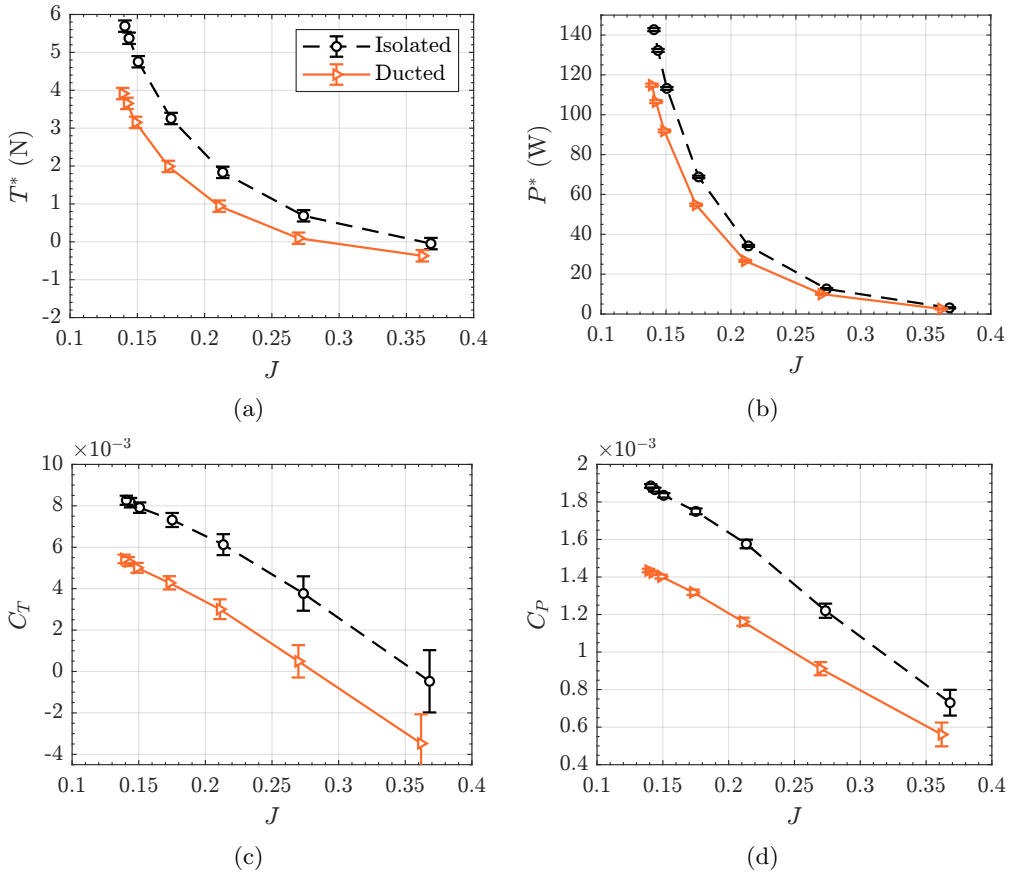

Figure 18. Measured thrust and power variations with advance ratio for isolated and ducted propeller configurations in simulated low-sped axial forward flight conditions.

4.1.3 Low-Fidelity Prediction Comparisons

Table 4 presents the comparison between SHAC measurements and DFDC predictions of the total thrust of the ducted propeller configuration and the thrust contributions of the propeller and duct components for hover conditions. As the table shows, DFDC does an excellent job at predicting the total thrust levels and relative thrust contributions of the duct and propeller components for operating conditions of $M_{\text{tip}} \geq 0.259$. Below this operating condition, DFDC overpredicts the thrust generated by the rotor and underpredicts the thrust generated by the duct. While the exact cause of this is unknown, it is believed to be due to incorrect estimations of drag induced by the duct as well as thrust generated by the propeller; both of which are believed to be related to low Reynolds number effects.

Table 5 provides a comparison between SHAC measurements and DFDC predictions of total system thrust and the thrust contributions of the propeller and duct components for low-speed axial flow conditions. As this table shows, the comparisons between DFDC predictions and SHAC measurements are slightly poorer than those for the static hover conditions at the lower tip speed operating conditions. Similar to the hover results of Table 4, the low-speed axial flow results show better agreement in total system thrust levels for $M_{\text{tip}} \geq 0.260$, with DFDC slightly over-

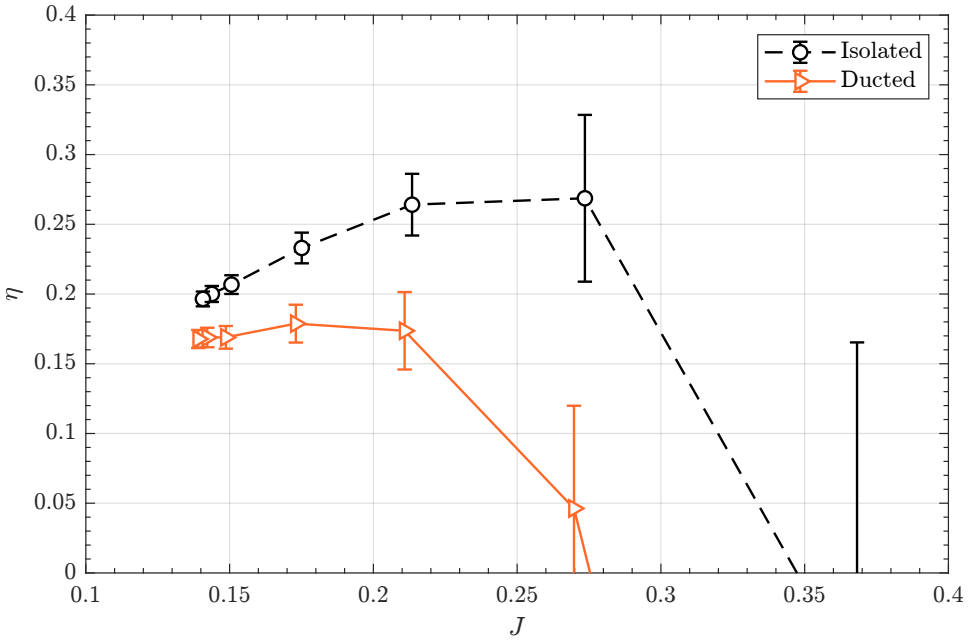

Figure 19. Propulsive efficiency variations with advance ratio for isolated and ducted propeller configurations in low-speed axial inflow conditions.

predicting the system thrust for all operating conditions. If attention is focused on the duct contributions of thrust in Table 5, it can be seen that there is an almost consistent offset in the thrust predictions as compared to the measurements. As mentioned previously, this could be related to surface roughness of the 3D printed blades and duct components as well as inaccurate drag modeling in DFDC itself. Another possible drag contribution in the experimental setup that is not present in the DFDC simulations is the load cell and duct support mounts. These components are visible in Figs. 5 and 8(b) for reference. Conceivably, these features could yield an increase in drag of the system under low-speed axial flow conditions that would not be captured by DFDC. Despite this, however, a nearly constant offset in this duct thrust prediction could be viewed as a consistent drag penalty that may be applied to the prediction; still rendering it a useful modeling tool. However, this

Table 4. Measured (SHAC) and predicted (DFDC) thrust values for the ducted propeller configuration in simulated hover conditions.

Operating Condition		T^*_{Total} (N)		T^*_{Prop} (N)		T^*_{Duct} (N)	
Ω^* (RPM)	M_{tip}	SHAC	DFDC	SHAC	DFDC	SHAC	DFDC
3207	0.124	0.97	1.40	0.48	0.96	0.49	0.44
4291	0.166	1.89	2.21	0.97	1.36	0.92	0.85
5500	0.213	3.19	3.31	1.62	1.79	1.57	1.52
6705	0.259	4.60	4.63	2.27	2.24	2.32	2.39
7808	0.302	6.17	6.26	3.00	3.00	3.17	3.26
8162	0.316	6.73	6.84	3.26	3.28	3.47	3.56
8383	0.324	7.04	7.22	3.37	3.46	3.66	3.76

Table 5. Measured (SHAC) and predicted (DFDC) thrust values for the ducted propeller configuration in low-speed axial flow conditions.

Operating Condition			T^*_{Total} (N)		T^*_{Prop} (N)		T^*_{Duct} (N)	
Ω^* (RPM)	M_{tip}	J	SHAC	DFDC	SHAC	DFDC	SHAC	DFDC
3214	0.124	0.38	-0.37	-0.05	-0.20	-0.04	-0.16	-0.01
4311	0.167	0.28	0.09	0.37	0.20	0.33	-0.10	0.05
5516	0.213	0.22	0.94	1.10	0.83	0.86	0.11	0.24
6722	0.260	0.18	1.99	2.12	1.55	1.54	0.45	0.58
7823	0.303	0.16	3.15	3.30	2.28	2.28	0.87	1.02
8178	0.316	0.15	3.65	3.74	2.58	2.55	1.08	1.19
8363	0.324	0.14	3.91	3.97	2.74	2.69	1.18	1.28

claim will need to be verified with additional test articles and operating conditions in the future.

Because DFDC demonstrated reasonable agreement with the measurements for both hover and low-speed axial flow conditions for the higher propeller tip speed operating conditions, it was further leveraged to visualize the modeled pressure and flow field behaviors. Figure 20 provides a comparison of the pressure distributions of the system components between the hover and low-speed axial inflow conditions at a common propeller tip speed of $M_{\text{tip}} = 0.324$. Note that the pressure distributions are presented in the form of vectors with amplitudes relative to a pressure coefficient $C_p = 1$ and directions that are normal to the body surfaces. This pressure coefficient follows conventional airfoil nomenclature of

$$C_p = \frac{P_s - P_\infty}{\frac{1}{2}\rho_\infty V_{\text{ref}}^2} = \frac{P_s - P_\infty}{Q_{\text{ref}}}, \tag{20}$$

where P_s is the surface pressure, P_∞ is the freestream or ambient pressure, ρ_∞ is the freestream or ambient density, and V_{ref} is the freestream velocity through the ducted propeller system. For the sake of simplicity, V_{ref} was defined as the average axial velocity through the propeller disk for a given simulation run, which is an output provided by the DFDC. This quantity was deemed an appropriate reference value so as to avoid the complication of zero freestream velocity associated with the hover operating conditions. A more quantitative representation of the pressure distributions on the nacelle, duct, and propeller surfaces are provided in Fig. 21. This figure reveals a prominent suction peak on the duct lower surface close to the leading edge of the duct ($x \approx 0.01$ m, or 6% of the duct chord) in the hover condition. Both duct and nacelle surfaces converge to $C_p = 0$ downstream of the propeller plane in hover. Furthermore, the hover propeller pressure distribution that is visible in Fig. 21(b) shows an increase in pressure along the blade span until it sharply drops off very close to the blade tip and duct inner surface. The low-speed axial inflow flight condition yields a reduction in the suction peak amplitude on the duct lower surface and shifts it further downstream. The duct upper surface also displays a stagnation point very close to the duct leading edge, with a value of $C_p \approx 0.2$, which corresponds to the dynamic pressure of the freestream velocity condition of $V_\infty = 5.2$ m/s. The pressure distribution of the propeller is also seen

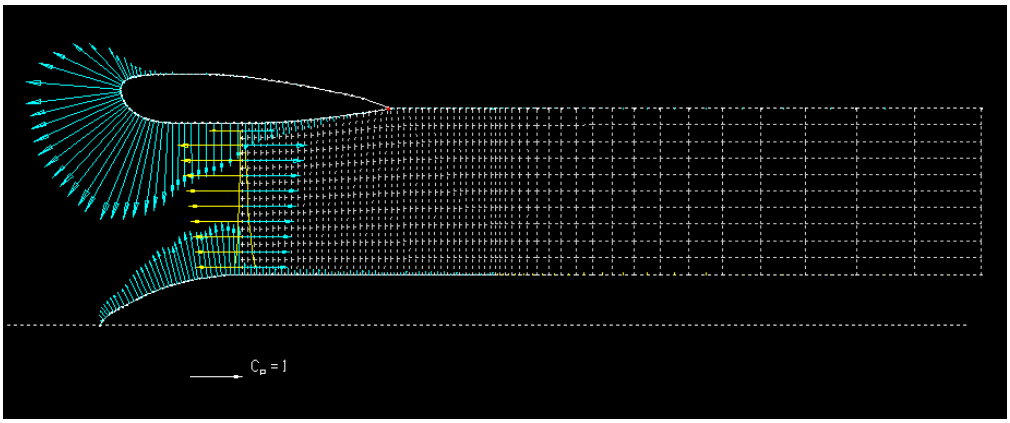

(a) Hover

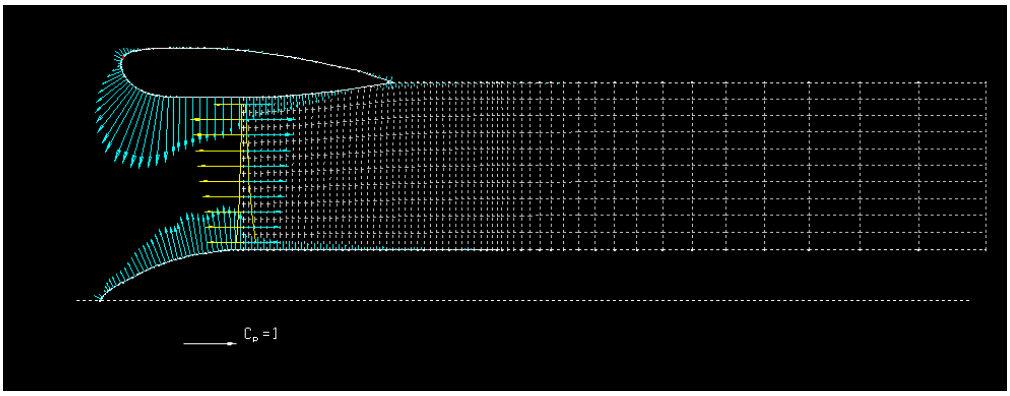

(b) Low-speed axial inflow

Figure 20. Pressure vectors along duct, propeller, and centerbody surfaces for (a) hover and (b) low-speed axial inflow conditions. *Note:* $M_{tip} = 0.324$ *for both figures.*

to decrease, corresponding to a thrust reduction associated with the incoming flow. The nacelle pressure distribution is seen to reduce slightly between the hover and low-speed axial inflow conditions, while a stagnation point emerges near the leading edge for the low-speed axial inflow condition. Both of these behaviors are associated with the imposed inflow freestream velocity, as opposed to the axial component of flow being solely attributed to the induced velocity of the propeller for the hover condition.

The mean flow field through the ducted propeller system predicted by the DFDC is visualized in Fig. 22 using streamlines. The hover results of Fig. 22(a) show streamlines representative of air particles being entrained around the duct leading edge from the upper surface to the lower surface as a result of the induced flow generated by the rotation of the propeller. This behavior changes for the low-speed axial inflow condition shown in Fig. 22(b), where the streamlines that originate above the duct are seen to progress along the duct upper surface rather than become entrained into the propeller. This is because the momentum of air particles in the freestream above the duct are outside of the reduced extents of the propeller

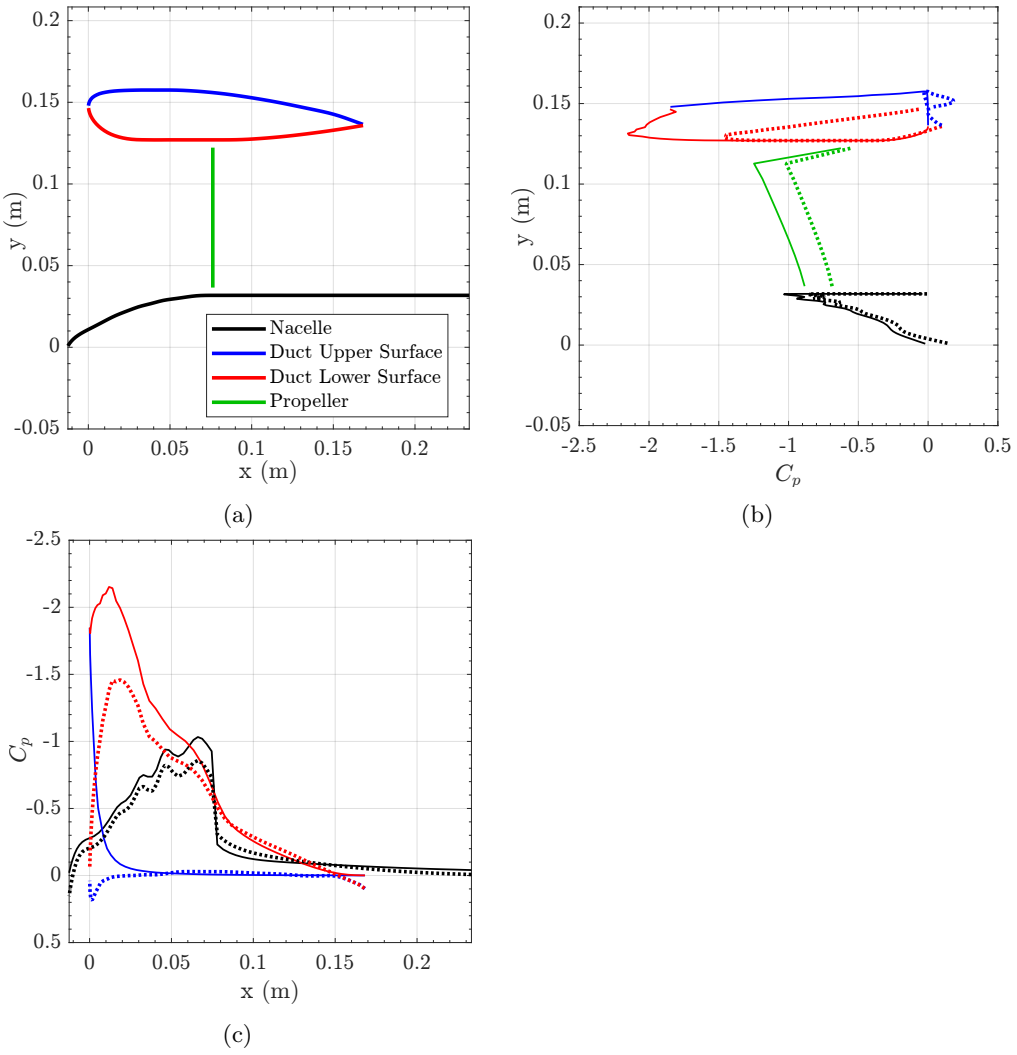

Figure 21. Pressure coefficient distributions on nacelle, duct, and propeller surfaces for hover and low-speed axial inflow conditions. *Note: M_{tip} = 0.324 for both conditions; hover condition represented by solid lines* ($V_{\text{ref}} = 11.6$ m/s)*, low-speed axial inflow condition represented by dotted lines* ($V_{\text{ref}} = 12.12$ m/s)*.*

slipstream, which is representative of the reduced thrust generated by the propeller as compared to the hover operating condition.

Overall, DFDC is shown to be an excellent modeling tool for the current application, with a total system thrust prediction being within 4% error relative to experiment for hover conditions with $M_{\text{tip}} \geq 0.213$, and within 6.5% error for low-speed axial flow conditions with $M_{\text{tip}} \geq 0.260$. It is also worth recalling the momentum theory prediction discussed previously in Section 3.2.1, which predicted a propeller and duct thrust contribution of 44% and 56% in hover, respectively. If the maximum tested rotation rate condition of $M_{\text{tip}} = 0.324$ is considered, the SHAC measurements yielded thrust contributions of 48% and 52% by the propeller and

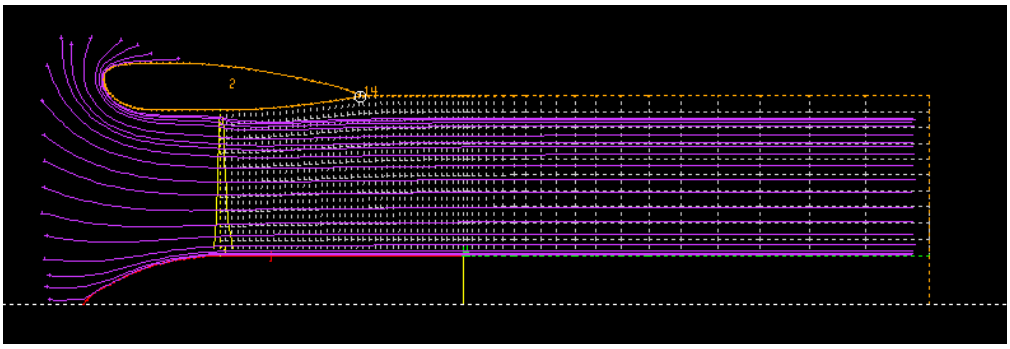

(a) Hover

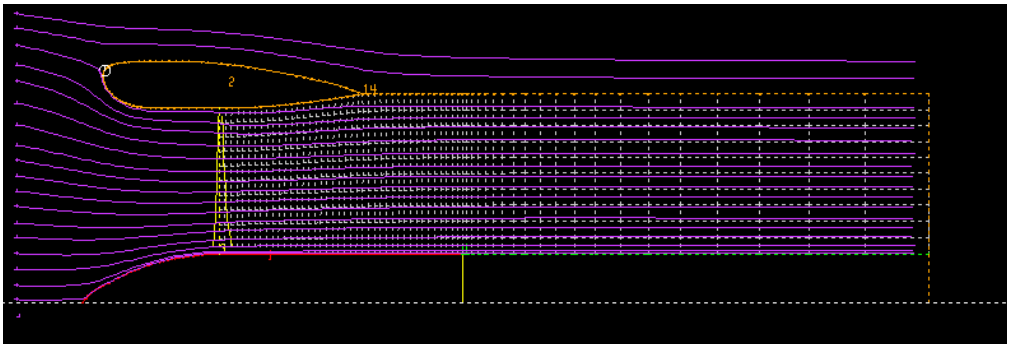

(b) Low-speed axial inflow

Figure 22. Mean velocity streamlines through the ducted propeller system predicted by the DFDC for (a) hover and (b) low-speed axial inflow conditions. *Note:* M_{tip} *= 0.324 for both figures.*

duct, respectively. Meanwhile, DFDC predicted thrust contributions of 48% and 52%, essentially identical to the experimental measurement relative contributions. Therefore, momentum theory and DFDC are shown to be good performance prediction methods, however with DFDC demonstrating both better accuracy and the ability to model axial forward flight conditions. Furthermore, the reasonably good agreement between experiment and DFDC predictions increases confidence for users of the DFDC for making and assessing ducted propulsor design improvements.

4.2 Acoustics

Acoustic assessment of the tested propulsor configurations is conducted in this section via several analysis techniques. As discussed in Section 2.4, periodic extraction is utilized in order to differentiate between the deterministic (periodic) and random (broadband) components of noise, which are presented in the forms of both narrowband spectra and integrated level directivities. In addition, the presence of noise contaminants by the brushless motor system is also discussed. This is an important consideration because it is a feature of the current test campaign that may be unique to such a small-scale testing configuration that may not directly translate to a UAM-scale vehicle.

The integrated overall sound pressure level (OASPL) directivities for the periodic, broadband, and raw acoustic data are computed across different frequency ranges. This is done in order to reduce the impacts of acoustic contaminants including microphone self-noise (a component of background noise) and tonal noise generated by the brushless motor. Both of these sources of noise contamination are discussed in the following sections. It is worth noting that the extracted periodic OASPL calculation is comprised of the narrowest frequency range of the three components. This is because of the presence of high-amplitude tonal noise generated by the brushless motor at certain frequencies both above and below this frequency range. Low-frequency tonal noise – notably at the shaft rotation rate of the motor – was found to be very prominent for the configurations in which the duct was present. Originally thought to be due to propeller blade imbalance effects, this was later proven to not be the cause when strong shaft harmonic acoustic amplitudes were observed for motor-only run conditions; in other words, conditions in which the duct was installed but with no propeller blades present. Therefore, this low-frequency tonal noise is attributed to a change in resonance of the propeller stand assembly with the addition of the duct support hardware. Therefore, the periodic OASPL contribution is computed as the sum of the acoustic energy in the first three BPF harmonics. Next, the residual noise OASPLs were computed starting at a cut-on frequency of approximately 1 kHz because this was the frequency at which propeller broadband noise was seen to occur above the facility background noise. The 30 kHz upper frequency limit was similarly defined as where the propeller broadband noise was seen to diminish and begin to coalesce with the system noise floor. Finally, the total OASPL is computed as the sum of the periodic and broadband OASPL components. Note that the broadband noise incorporated into this total OASPL (L_{Total}) retained the remnant tones present in the residual spectra. This was done in order to maintain consistency in post-processing between the hover and low-speed axial inflow test conditions, the latter of which contain high levels of remnant tonal energy in the residual spectra. It was deemed appropriate by the authors to include these levels in the total OASPLs in order to perform a fair comparison between the two propeller configurations.

4.2.1 Hover

Figures 23 and 24 provide the narrowband acoustic spectra at an observer angle of $\theta_o = -35°$ for the isolated and ducted propeller configurations in hover, respectively. Specifically, Figs. 23(a) and 24(a) show the raw narrowband acoustic spectra for several tip speed operating conditions with the first three extracted BPF harmonics superimposed, Figs. 23(b) and 24(b) show the residual broadband spectra after periodic extraction for the same operating conditions, and finally Figs. 23(c) and 24(c) show the residual broadband spectra for all tested tip speed conditions with remnant tones removed. Note that all spectra are plotted with a 16 Hz frequency resolution and are corrected to a common arc distance of 1.91 m using spherical spreading (denoted by $[\ ]^*$).

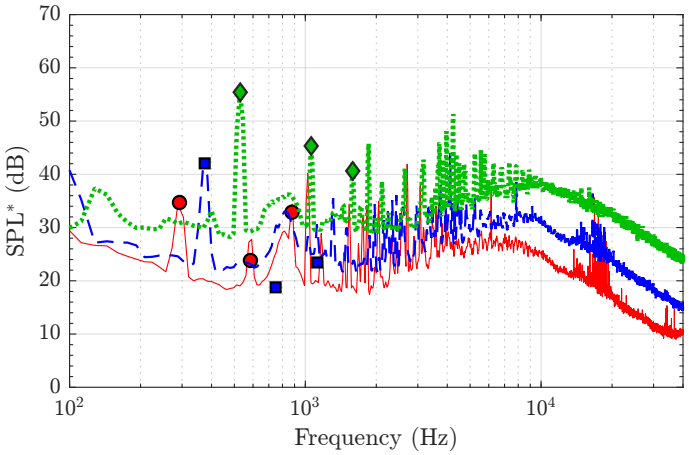

(a) Raw Spectra with BPF Harmonics

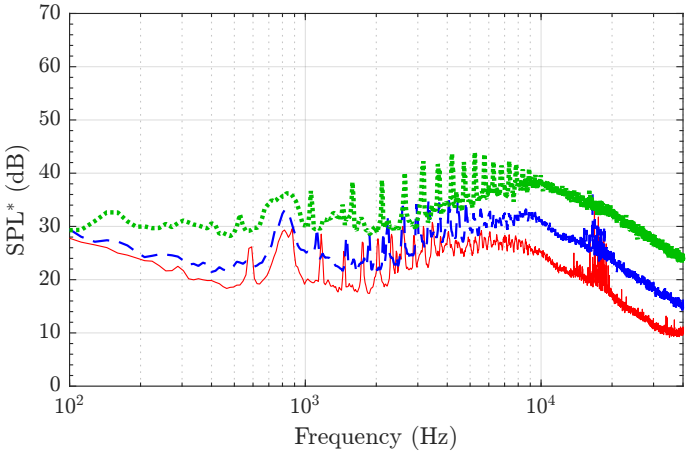

(b) Extracted Broadband Spectra

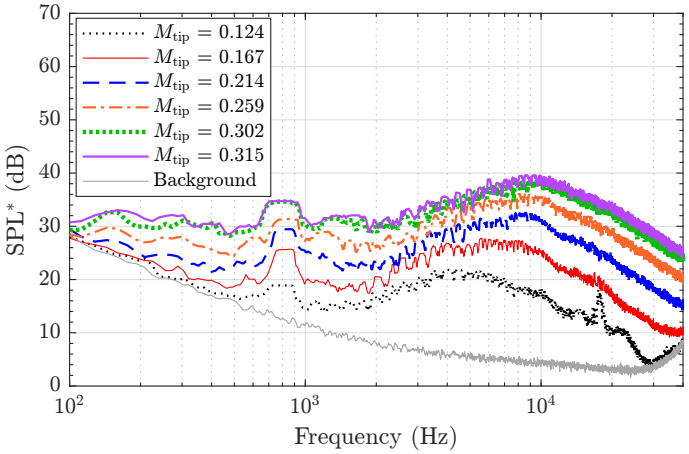

(c) Broadband Spectra with Remnant Tones Removed

Figure 23. Acoustic spectra for different post-processing methods at $\theta_o = -35°$ (microphone 6), for the isolated propeller in simulated hover conditions.

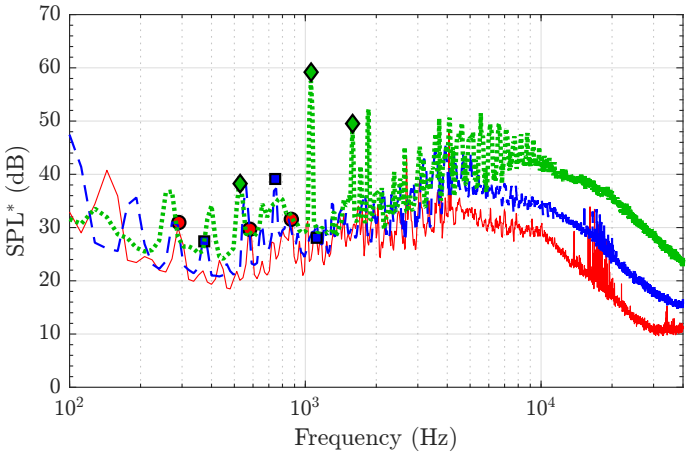

(a) Raw Spectra with BPF Harmonics

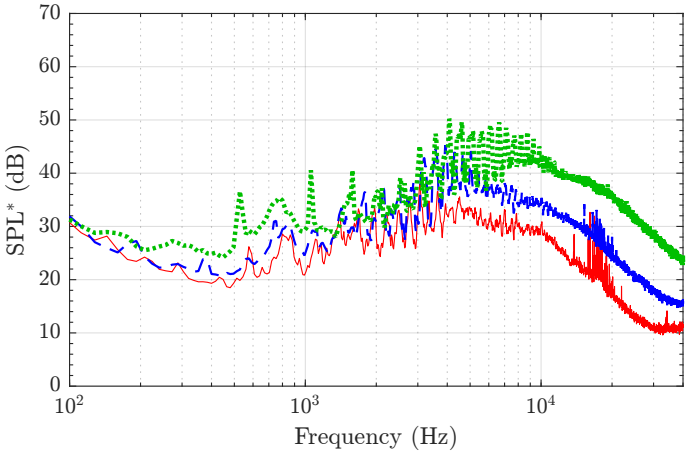

(b) Extracted Broadband Spectra

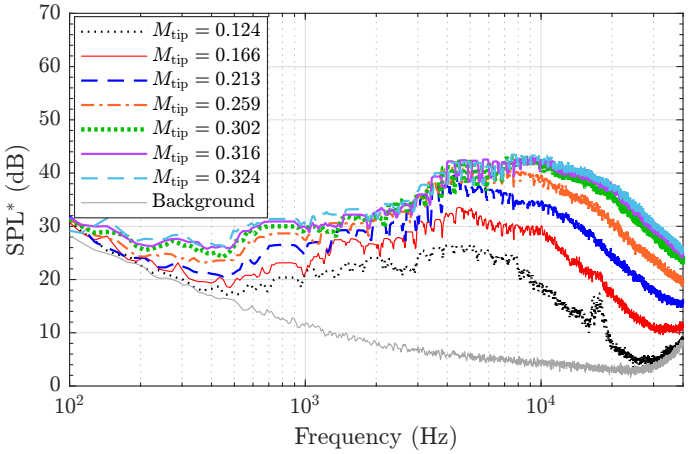

(c) Broadband Spectra with Remnant Tones Removed

Figure 24. Acoustic spectra for different post-processing methods at $\theta_o = -35°$ (microphone 6), for the ducted propeller in simulated hover conditions.

If attention is focused on Figs. 23(a) and 24(a), it can be seen that the isolated propeller exhibits an overall increase in the amplitude of the BPF harmonics with increasing tip speed, with the BPF itself being the strongest tonal component for each run condition. This is expected for rotors and propellers with moderate disk loading. Meanwhile for approximately the same set of tip speed conditions, the ducted propeller exhibits BPF amplitudes of reduced amplitude, with overall higher amplitudes for the second and third BPF harmonics as compared to those of the isolated propeller. As for the extracted broadband components of the spectra, Figs. 23(b) and 24(b) show an increase in the peak broadband levels for the common tip speed conditions, also with increased levels of remnant tones. These increased levels are believed to be associated with turbulence interactions between the propeller blade tip regions and the duct wall, potentially caused by flow separation along the duct inner surface. As was shown in Section 4.1.1, the propeller blades themselves generate considerably less thrust in the ducted configuration, likely due to this flow separation. The increase in broadband levels exhibited by the ducted propeller relative to the isolated propeller is observed across all operating conditions between Figs. 23(c) and 24(c).

In an attempt to quantify the sources of broadband noise on the current test article, a prediction is performed using the ANOPP2 Self-Noise Internal Functional Module (ASNIFM) [31, 32]. This module is intended to predict the self-noise generated by rotating blade systems and is based on the semiempirical prediction method applied to airfoils across a wide range of Reynolds numbers and angles of attack [33]. This prediction toolchain models five airfoil self-noise mechanisms related to specific boundary layer phenomena:

- Boundary-layer turbulence passing the suction and pressure sides of the airfoil trailing edge (**TBL**$_s$ and **TBL**$_p$, respectively)
- Separated boundary layer and stalled airfoil flow (**TBL**$_\alpha$)
- Vortex shedding due to laminar boundary layer instabilities (**LBL-VS**)
- Vortex shedding from blunt trailing edges (**BVS**)
- Turbulent vortex flow near the tips of lifting blades (**TVF**)

Figure 25 provides a comparison between the measured broadband noise generated by the isolated propeller at a mid-range tip speed condition in hover and the associated ASNIFM prediction. The ASNIFM prediction was performed utilizing a tripped blade assumption, which was deemed to be appropriate based on the notion that flow over the blade is fully turbulent (see Section 4.1.1). As a result, the prediction does not include a LBL-VS source noise component. Note that the experimental data are represented by the residual spectra with remnant tones removed. Figure 25(a) presents the spectra in 1/3rd octave bands, which is the native format of the prediction data output by ASNIFM. As this figure shows, there is overall excellent agreement in spectral trends between the total prediction (comprised of the sum of the five individual sources shown) and the experimental measurement for frequencies at and above 2 kHz, with a nearly consistent underprediction across

all frequencies. This underprediction could be related to the remnant tone removal process retaining unwanted energy in the spectrum. The prediction indicates that the dominant source mechanisms are TBL_s, TBL_p, and BVS, in order of increasing frequency. Furthermore, it is worth noting that the contribution of boundary layer separation or stall (TBL_α) is not predicted to be a principal self-noise contributor. This makes sense because the blade is designed to have a constant angle of attack of 3.25° along the blade span, for which the flow over a NACA 0012 airfoil is expected to remain attached. Figure 25(b) shows the directivity comparison between SHAC measurements and ASNIFM predictions of the 1/3rd octave band integrated broadband noise at the same operating condition, summed over the frequency range $2 \leq F_c \leq 31.5$ kHz. While the levels are slightly off due to an overall consistent underprediction in spectral levels, the trends agree very well.

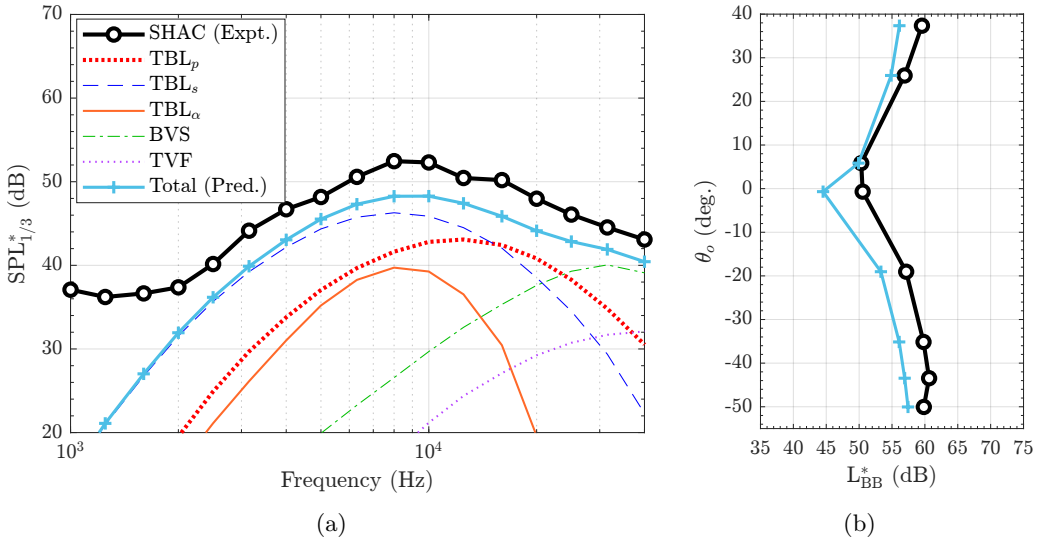

Figure 25. Comparisons between broadband self-noise predictions using ASNIFM and SHAC experimental measurements of the isolated propeller in hover operating at at $\Omega = 5613$ RPM ($M_{\mathrm{tip}} = 0.214$): (a) 1/3rd octave-band spectra comparisons at $\theta_o = -35°$ (microphone 6), (b) integrated broadband noise OASPL directivities.

Figures 26 and 27 show the directivities of the different extracted noise components for the tested propeller configurations in hover. If attention is focused on Figs. 26(a) and 27(a), it can be seen that there is an almost consistent reduction in the SPL at the BPF across all observer angles between isolated and ducted configurations for common tip speed conditions. It is also worth noting that while the BPF directivity for the isolated propeller in Fig. 26(a) is seen to converge to a trend that is typical of light- and moderately-loaded rotors [22], the BPF directivity for the ducted propeller in Fig. 27(a) is dramatically different in shape. It is possible that the duct could be providing shielding of these pressure waves. This speculation is supported by the PAS BPF acoustic predictions in Section 3.1 (Fig. 12), which showed that the acoustic amplitude at this deterministic frequency was dominated by steady thickness noise. This would imply that the noise reduction at the BPF

due to the added presence of the duct would be the result of acoustic shielding and not due to the reduced aerodynamic loading generated by the propeller blades. This benefit is negated, however, when considering the tonal OASPL directivities in Figs. 26(b) and 27(b), as well as the broadband (with remnant tones removed) OASPL directivities in Figs. 26(c) and 27(c). While there are tip speed conditions for which the ducted propeller exhibits reduced tonal noise when compared to the isolated rotor, there is a considerable increase in broadband OASPLs for nearly all observers.

A preliminary attempt at broadband spectral scaling is applied in Figs. 26(d) and 27(d) based on documented self-noise scaling behaviors discussed in Reference 33. Based on the prediction comparison results in Fig. 25, it might be expected that the broadband noise of the isolated propeller would scale according to that documented for turbulent boundary layer trailing edge noise. As indicated in Reference 33, one possible scaling convention is

$$\text{Scaled } \text{SPL}_{1/3} = \text{SPL}_{\text{TBL}} - 10\log_{10}\left(M^5 \frac{\delta^* L}{r_e^2}\right), \tag{21}$$

where M represents the characteristic Mach number, δ^* is the displacement thickness, L is a representative spanwise length scale, and r_e is the effective observer distance from the source. This expression can be simplified, however, utilizing some assumptions regarding the propeller design. Because the propeller is designed as an optimal hovering rotor, then the angle of attack ideally remains constant along the blade span and with changing rotation rate. In addition, if one considers the 75% spanwise location of the blade for reference, then the airfoil at this location experiences Reynolds numbers of $54,000 \leq Re_c \leq 136,000$ over the range of tested rotation rates in this study. This is a range of Reynolds numbers for which the displacement thickness measurements at zero angle of attack of Reference 33 showed very little variation. This coupled with the assumption of a nearly invariant angle of attack with blade rotation rate suggests the removal of the dependency of Eq. 21 on displacement thickness. In addition, because the blade and observer geometries also remain constant between operating conditions, the only remaining parameter of variation in Eq. 21 is Mach number. The equation can then be rewritten as a ratio of a tip Mach operating condition relative to a reference value, or

$$\text{Scaled } \text{SPL}_{1/3} = \text{SPL}_{1/3} + 10\log_{10}\left(\frac{M_{\text{ref}}}{M_{\text{tip}}}\right)^n, \tag{22}$$

where the exponent n would be set to a value of $n = 5$ to correspond to the scaling convention of Eq. 21. This expression can be similarly applied to the integrated broadband OASPL as

$$\text{Scaled } \text{L}_{\text{BB}} = \text{L}_{\text{BB}} + 10\log_{10}\left(\frac{M_{\text{ref}}}{M_{\text{tip}}}\right)^n. \tag{23}$$

The result of this scaling applied to the broadband OASPL directivities for the isolated propeller shown in Fig. 26(d) shows excellent collapse of the data, with the exception of the observer at $\theta = 5.7°$ for the lowest tested rotation rate condition.

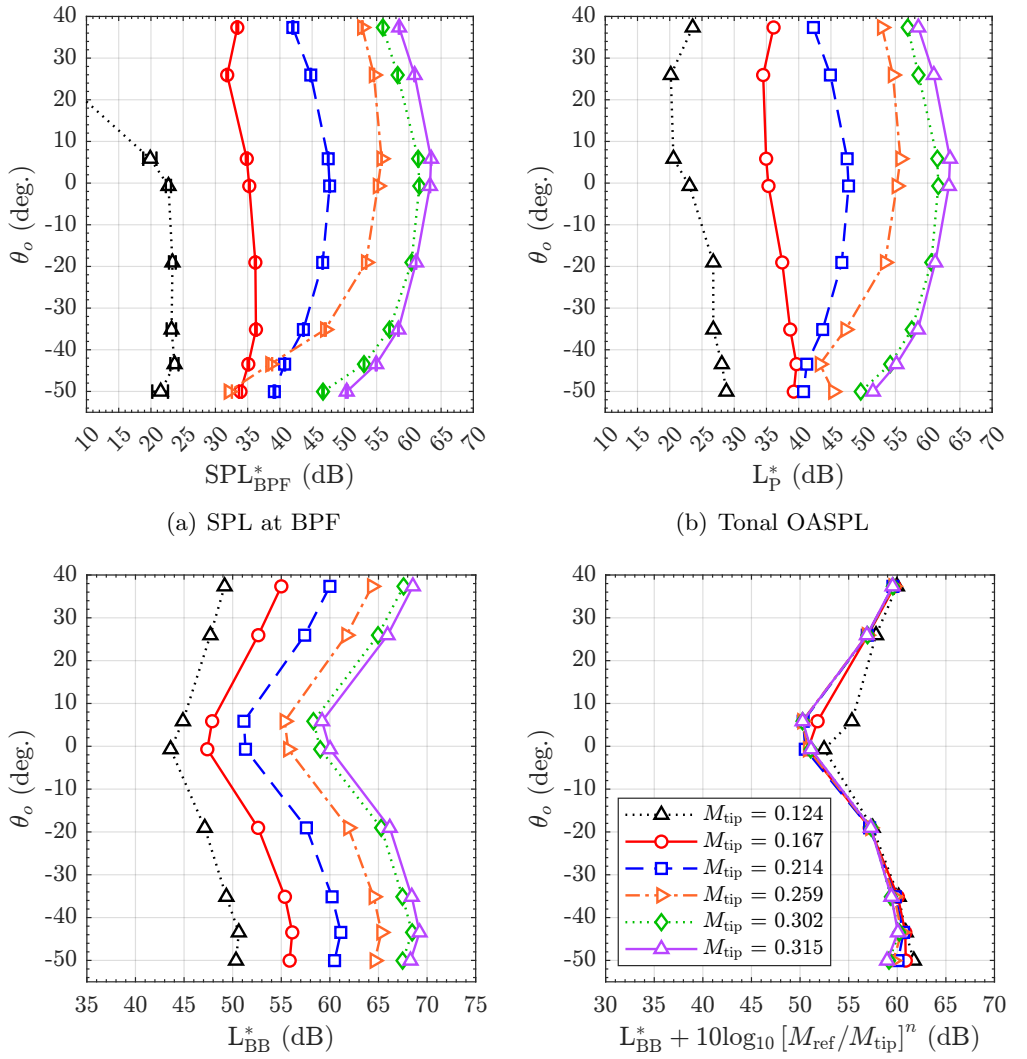

(a) SPL at BPF

(b) Tonal OASPL

(c) Broadband OASPL (Tones Removed)

(d) Scaled Broadband OASPL (Tones Removed)

Figure 26. Acoustic directivities for the isolated propeller in simulated hover conditions. Note broadband noise scale factor set to $\mathbf{n = 5}$.

This was found to be due to very poor SNR at this operating condition. This excellent data collapse provides further evidence as to the nature of this broadband noise being primarily due to turbulent boundary layer fluctuations. A similar collapse in the ducted propeller data is seen in Fig. 27(d), however with a reduced Mach number power ratio of $n = 4.5$ instead of $n = 5$. While the exact cause of this is unknown, it is believed to be due to additional broadband noise generation due to the ingestion of turbulent flow along the duct inner surface into the propeller tip region. As a result, it is reasonable to expect the broadband OASPLs to scale differently due to the combination of the different broadband noise-generation mechanisms.

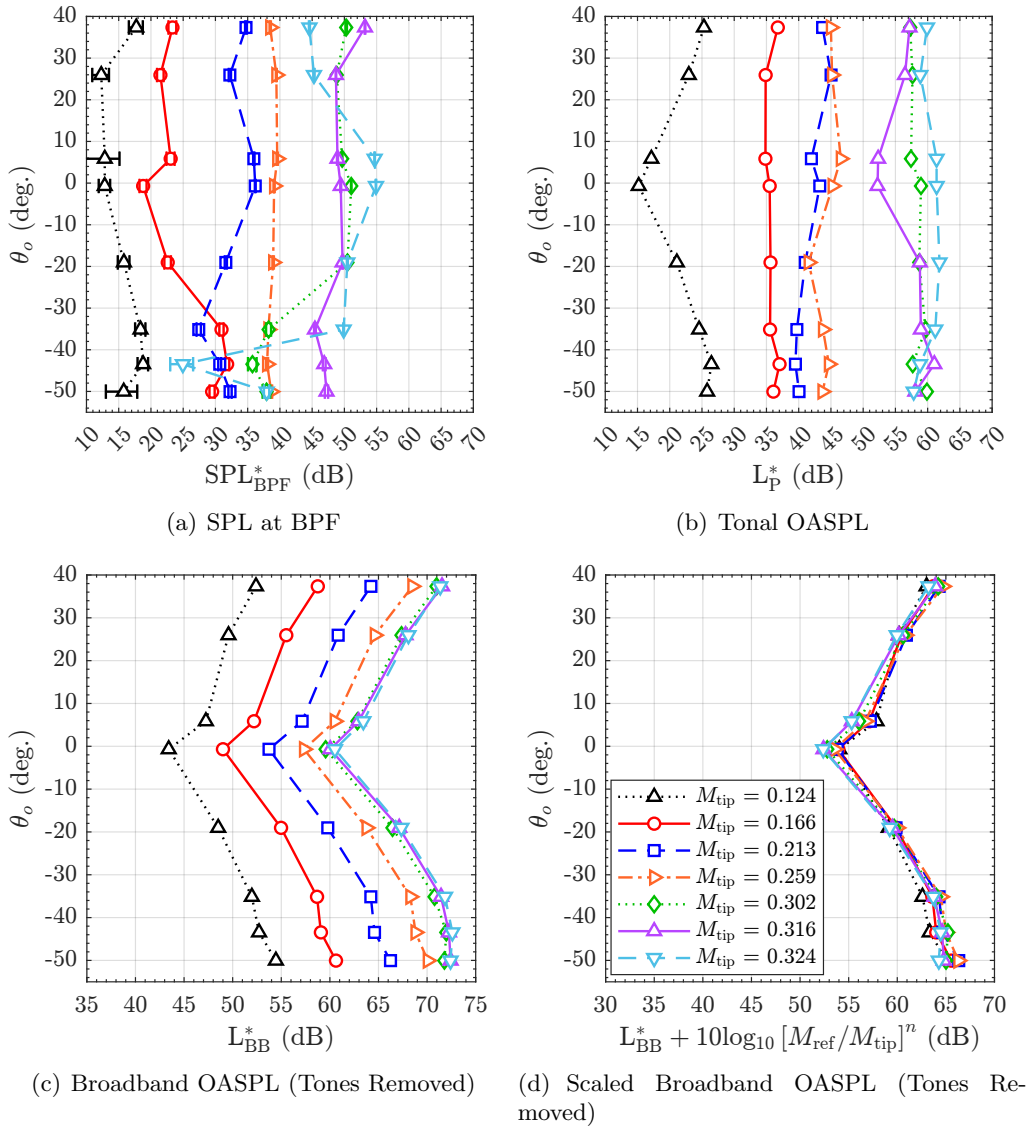

(a) SPL at BPF

(b) Tonal OASPL

(c) Broadband OASPL (Tones Removed)

(d) Scaled Broadband OASPL (Tones Removed)

Figure 27. Acoustic directivities for the ducted propeller in simulated hover conditions. Note broadband noise scale factor set to $\mathbf{n = 4.5}$.

Figure 28 presents an acoustic comparison between the isolated and ducted propeller configurations at a common net thrust condition in hover. As is indicated in Fig. 28(a), the propeller in the ducted configuration needed to be rotated at a 4.6% faster rate for the total system thrust to equal that of the isolated propeller. The spectra of Fig. 28(a) show a considerable reduction in the BPF acoustic amplitude for the ducted propeller as compared to the isolated, however an increase in the second and third harmonics. There is also an increase in the remnant tone content and in the overall broadband noise spectral shelf. The total OASPL directivity results of Fig. 28(b) furthermore show increases between 2.5 and 7 dB at out-of-plane observers. However, there is a slight reduction in total OASPL at the in-plane observer location. This is indicative of the tonal noise reduction benefit offered by the

ducted propeller configuration at an observer location of lowest broadband noise levels, which was shown previously in Figs. 26(b) and 27(b).

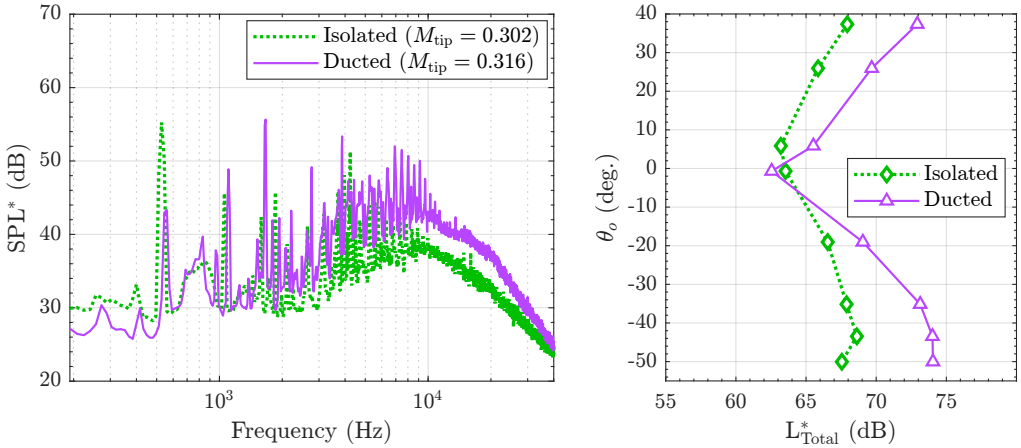

(a) Raw Acoustic Spectra ($\theta_o = -35^\circ$)

(b) Total OASPL Directivities

Figure 28. Out-of-plane acoustic spectra and total OASPL directivity comparisons between isolated and ducted propellers at common thrust conditions in hover.

4.2.2 Low-Speed Axial Flow

Figures 29 and 30 provide narrowband acoustic spectra for the isolated and ducted propeller configurations in low speed axial flow, respectively. The extracted BPF harmonics for the isolated propeller in Fig. 29(a) show a harmonic roll-off behavior typically observed for propellers in axial forward flight at light to moderate disk loading. Conversely, Fig. 30(a) shows reduced amplitude of the fundamental BPF and increased levels at the second and third harmonics relative to the isolated propeller, similar to the hover results presented in the previous section. The fact that this trend of BPF amplitude reduction and higher harmonic amplification is common between the two flow condition scenarios (hover and low-speed axial flow) with the addition of the duct to the isolated propeller, provides evidence that this phenomenon is tied to the duct presence itself. In other words, the presence of the duct has a common shielding/scattering behavior related to the frequency content of the propeller system, regardless of the change in net thrust of the system between flight conditions. However, this behavior would likely change at higher freestream flow conditions.

The extracted spectra of Figs. 29(b) and 30(b) show prominent residual "tones", which were not removed during the periodic extraction process. The primary cause of this is related to turbulence ingestion [34]. As discussed in Section 2.2, the freestream turbulence intensity of the core flow has been previously measured to be rather high ($TI = 4.2\%$). As a result of this, the BPF and its associated harmonics are "excited" by turbulent eddies that are axially stretched as they are pulled into the propeller's contracting slipstream. The propeller blades then cut through these stretched eddies that result in pressure perturbations that are experienced in the leading edge region of the blade. These pressure perturbations occur at harmonics of the blade passing frequency, the frequency extents of which are related to the axial and radial extents of the ingested turbulent structures. A similar harmonic excitation occurs with rotor wake recirculation, when the rotor ingests turbulent structures previously shed from its own wake. This effect is illustrated for the SHAC facility in Refs. [19] and [35], and the reader is referred to Ref. [20] for more information on this phenomenon. While some progress has recently been made on modeling this behavior in the current setup, the remnant tone removal process previously discussed is a simple attempt implemented in this study to remove this unsteady loading noise source from the data.

Figures 29(c) and 30(c) show the broadband spectra with remnant tones removed for the isolated and ducted propeller for low-speed axial flow conditions, respectively. This noise behavior is fairly similar between the two propeller configurations, however the ducted propeller exhibits slightly higher frequency peak broadband noise levels.

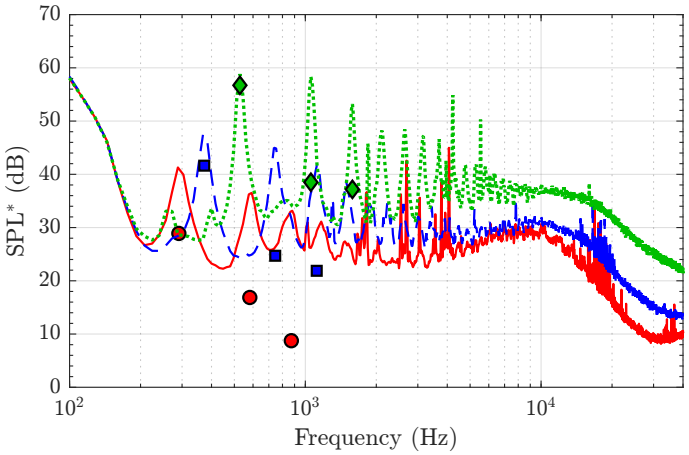

(a) Raw Spectra with BPF Harmonics

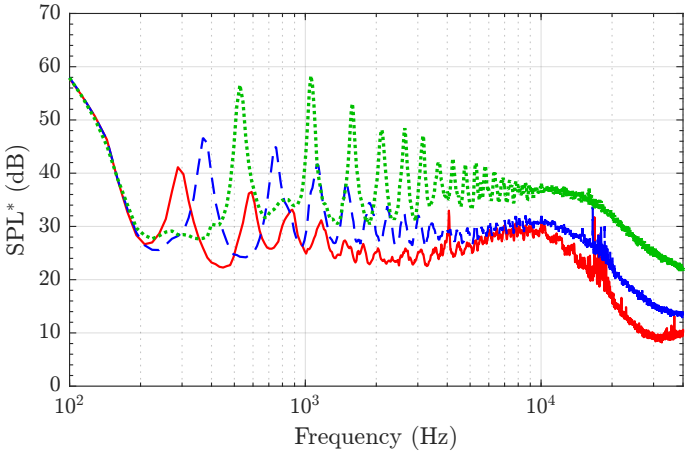

(b) Extracted Broadband Spectra

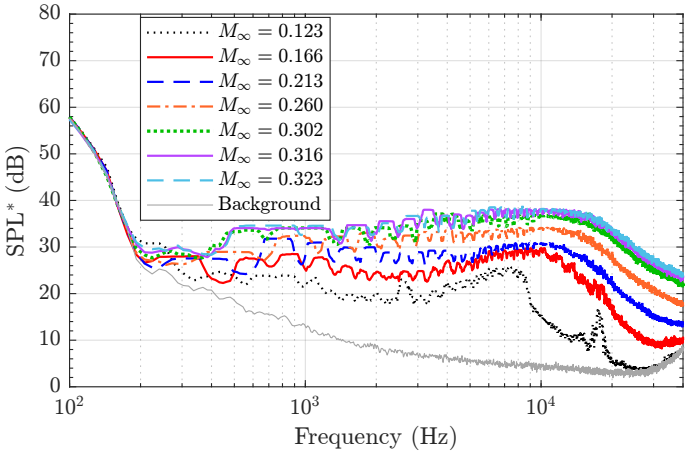

(c) Broadband Spectra with Remnant Tones Removed

Figure 29. Acoustic spectra for different post-processing methods at $\theta_o = -35°$ (microphone 6), for the isolated propeller in low-speed axial flow conditions.

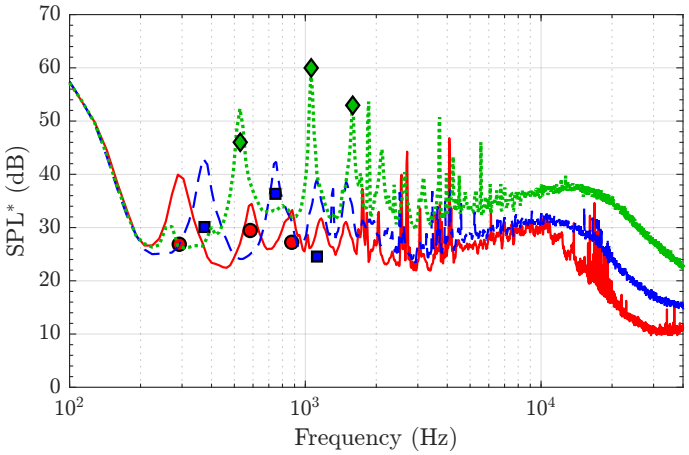

(a) Raw Spectra with BPF Harmonics

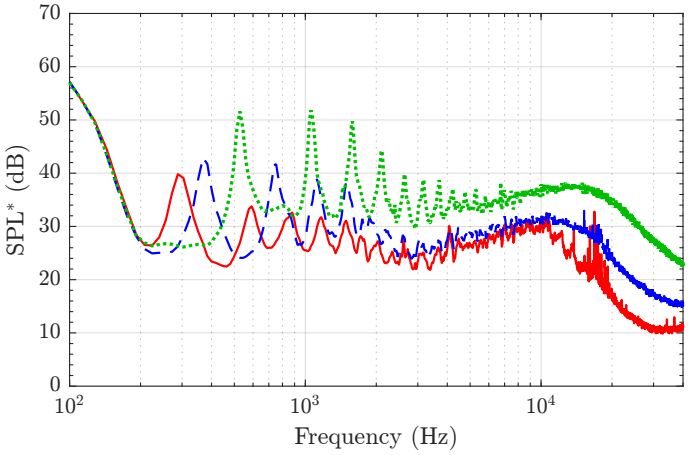

(b) Extracted Broadband Spectra

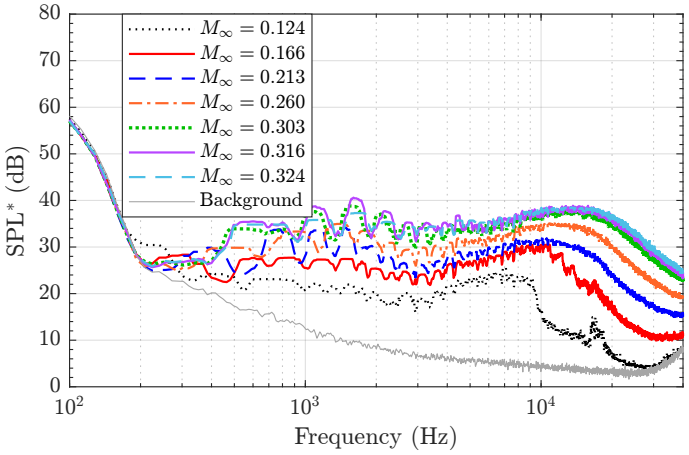

(c) Broadband Spectra with Remnant Tones Removed

Figure 30. Acoustic spectra for different post-processing methods at $\theta_o = -35°$ (microphone 6), for the ducted propeller in low-speed axial flow conditions.

Figures 31(a) and 32(a) show the BPF SPL directivities across the range of tested rotation rates for the isolated and ducted propeller configurations in low-speed axial flow conditions, respectively. Similar to the hover results shown in the previous section, a reduction in this SPL is observed at common rotation rates for most of the observer angles for the ducted propeller relative to the isolated propeller. This is again believed to be related to a shielding effect of the radiated thickness noise of the propeller offered by the duct presence. This speculation is further enforced by the PAS prediction of this acoustic amplitude in Section 3.1. While the prediction in Fig. 12 is representative of the hover condition of the isolated propeller, the thickness noise remains approximately unchanged between the hover and low-speed axial flow

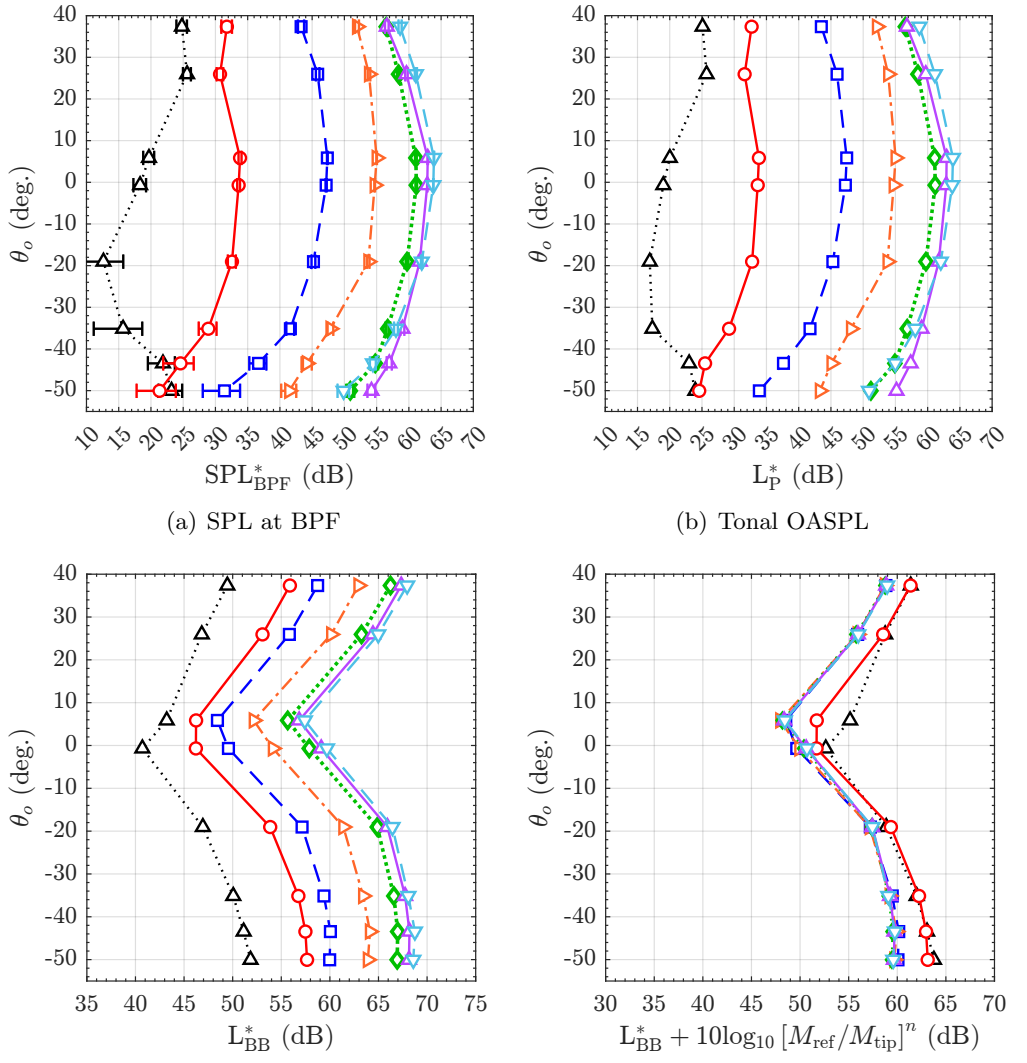

(a) SPL at BPF

(b) Tonal OASPL

(c) Broadband OASPL (Tones Removed)

(d) Scaled Broadband OASPL (Tones Removed)

Figure 31. Acoustic directivities for the isolated propeller in low-speed axial flow conditions. Note broadband noise scale factor set to $\mathbf{n = 5}$.

conditions. Therefore, the propeller steady thickness noise is believed to remain the primary noise component for the low-speed axial flow cases, especially due to the reduced aerodynamic loading generated by the propeller in this operating condition relative to hover.

Figures 31(b) and 32(b) show the tonal OASPL directivities for the isolated and ducted propellers in axial forward flight, respectively. Similar to the results for the hover conditions, it is difficult to identify a definitive trend between the two propeller configurations in these figures. This is likely due to a complex acoustic scattering behavior due to the presence of the duct that warrants further investigation.

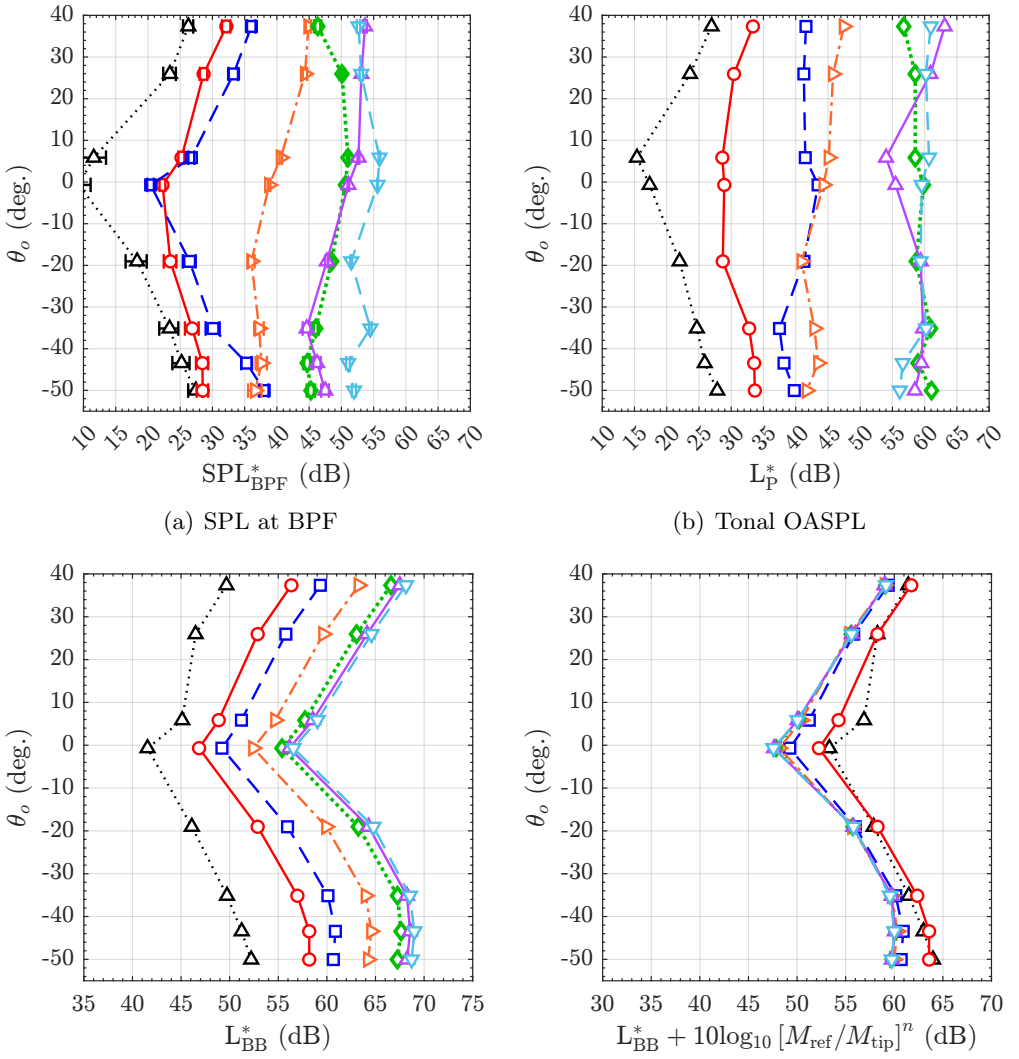

(a) SPL at BPF

(b) Tonal OASPL

(c) Broadband OASPL (Tones Removed)

(d) Scaled Broadband OASPL (Tones Removed)

Figure 32. Acoustic directivities for the ducted propeller in low-speed axial flow conditions. Note broadband noise scale factor set to $\mathbf{n = 5}$.

Figures 31(c) and 32(c) provide the integrated broadband noise directivities with remnant tones removed for the isolated and ducted propeller configurations in low-speed axial flow, respectively. In contrast to the results for these quantities in hover, there is very little difference in the integrated broadband noise between the isolated and ducted propeller in low-speed axial flow. This is believed to be due to much better flow attachment along the inner duct surface for the axial flow case. This can be qualitatively observed in Fig. 22 where the hover streamlines of Fig. 22(a) are seen to detach from the duct inner wall, including near the propeller tip region. This is contrasted by Fig. 22(b), where the streamlines are seen to remain attached to the duct inner surface in the vicinity of the propeller tip. As was shown in Figs. 29(b) and 30(b), the most notable difference in the peak-removed broadband noise spectra with the inclusion of the duct is a slight increase in the peak frequency content at higher rotation rate operating conditions. The exact cause of this behavior is currently unknown and is complicated by the likely complex scattering and shielding behavior offered by the duct.

Figures 31(d) and 32(d) show the scaled integrated broadband noise level directivities using a 5^{th} power of tip Mach scaling ($n = 5$) for the isolated and ducted propeller in low-speed axial inflow conditions, respectively. It is worth recalling that these integrations are performed over a frequency range of $992 \leq F \leq 30,000$ Hz based on signal-to-noise limitations, and that they are performed on the remnant tone-removed residual spectra. In both configurations, the system demonstrates good collapse of the broadband noise data, except for the two lowest tip speed conditions. While the exact cause of this is not known, it is worth recalling the aerodynamic performance results of Section 4.1.2, which demonstrated either negative thrust or extremely low positive thrust levels generated by the isolated and ducted configurations. This is due to reduced angles of attack experienced by the blade sections as a result of the incoming freestream flow through the facility. As a result, portions of the propeller blades generating negative thrust (positive drag) could exhibit aberrant broadband noise scaling behaviors.

Figure 33 provides an acoustic comparison between the isolated and ducted propeller configurations operating in low-speed axial flow at common system thrust output conditions. Figure 33(a) provides a raw acoustic spectra comparison at microphone 6 ($\theta_o = -35°$). This figure demonstrates the higher-frequency BPF harmonics associated with the ducted propeller configuration, which is indicative of the higher rotation rate needed to overcome the drag of the system. Specifically, the ducted propeller had to operate 16.5% faster than the isolated propeller to achieve the same thrust. It is worth recalling that the hover conditions analyzed in the previous section revealed a 4.6% rotation increase needed for the ducted propeller to match the thrust of the isolated propeller. Figure 33(b) meanwhile shows the total OASPL directivities of the two configurations. The ducted propeller is seen to exhibit higher overall noise levels (an average of 3 dB) across all observer locations. It is worth noting that these OASPL values were calculated as the sum of the periodic components of noise (first 3 BPF acoustic amplitudes) and residual component, which includes the remnant tonal data. This remnant tonal data is evidenced to be primarily the result of turbulence ingestion noise, which can potentially obscure the results. However, a very similar calculation was made using the remnant tone-

removed residual spectra, which showed very similar relative trends between the two propulsor configurations. Overall, the reduced efficiency of the ducted propeller in low-speed axial flow is seen to also correspond to higher overall noise levels relative to the isolated propeller at common thrust settings.

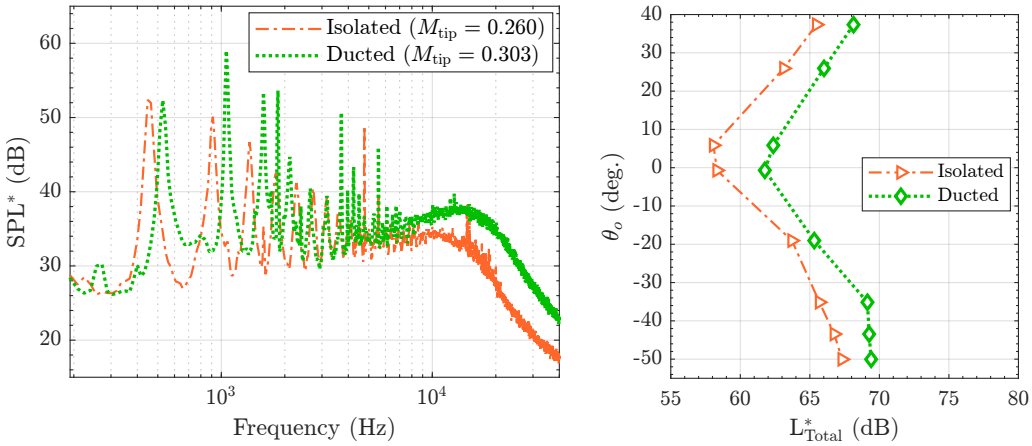

(a) Raw Acoustic Spectra ($\theta_o = -35°$)

(b) Total OASPL Directivities

Figure 33. Out-of-plane acoustic spectra and total OASPL directivity comparisons between isolated and ducted propellers at common thrust conditions in low-speed axial flow.

5 Concluding Remarks

The aerodynamic and acoustic performance trade-offs of a ducted propeller system were assessed relative to an isolated (open) propeller in this study using experimental and low- to mid-fidelity modeling methods. It was found that the isolated propeller aerodynamic and acoustic performance could be reasonably modeled using tools in the ANOPP suite. Furthermore, the ducted propeller aerodynamic performance could be modeled reasonably well using both momentum theory for hover operations, and the DFDC for both hover and low-speed axial inflow conditions.

From an aerodynamic performance perspective, the ducted propeller configuration was found to generate more thrust per unit of power draw (power loading) than the isolated propeller configuration in hover conditions. This is because the induced flow generated by rotation of the propeller blades yields a pressure differential along the duct surface that results in thrust generation by the duct itself. This behavior was effectively modeled using momentum theory and the DFDC. It was found, however, that the propeller needed to operate at a faster rotation rate with the duct present to match the thrust condition of the isolated open propeller. Specifically, the data points analyzed revealed a necessary 4.6% increase in the propeller rotation rate with the duct present to match the isolated propeller thrust. As for the low-speed axial inflow conditions, the ducted propeller was found to perform considerably worse than the isolated one. This is due to the large amount of drag generated by the duct due to freestream flow over the duct surface. As a result, the propeller needed to operate 16.5% faster in order to match the thrust generated by the isolated propeller.

For common thrust generation between the two configurations in both hover and low-speed axial inflow, the ducted propeller was found to exhibit higher overall noise levels than the isolated propeller for nearly all observer locations. In hover, this was found to be primarily due to an augmentation of the higher BPF harmonics and an increase in broadband noise. The exact causes for the excitation of the higher BPF harmonics are not currently known, however they are believed to be related to the complex scattered acoustic field generated by the duct presence. The increase in broadband noise is believed to be related to separated flow along the inner duct surface interacting with the propeller blade tips. As for the low-speed axial inflow conditions, the increase in noise was seen to be primarily due to the BPF higher harmonic augmentation effect, and only slightly due to increased broadband noise levels. The additional increase in required rotation rate of the ducted propeller to match the thrust of the isolated propeller partially contributes to the increased tonal amplitudes. Despite this, some interesting effects were observed due to the presence of the duct. The ANOPP-PAS code showed good agreement with isolated propeller experimental data, which confirmed that the majority of tonal noise generated by the isolated propeller at the BPF is due to steady thickness noise. Furthermore, comparison between isolated and ducted propeller configurations for common rotation rate (tip speed) conditions, reveal a prominent shielding effect offered by the presence of the duct at the BPF. This benefit is negated, however, by the increase in higher BPF harmonic levels. The slight increase in broadband noise levels of the ducted propeller is believed to be simply due to the increased tip speed operating

condition, which would yield higher angles of attack along the blade, and thus higher levels and frequency content of blade self-noise. The apparent presence of turbulence ingestion was found to yield prominent levels of residual tonal noise for both tested configurations. While this does affect the overall integrated noise level directivities, removal of these residual tones to yield a residual spectrum was found to yield very similar comparative trends between the isolated and ducted propellers. Methods for predicting and modeling turbulence ingestion noise into a rotor are currently being tested and are left for future work.

While there were observed higher noise levels and poorer aerodynamic performance of the ducted propeller system under certain operating conditions, additional work is warranted. For example, the design of the duct used in this study was a first-pass based on reference material for a much larger propulsor platform, and could serve to be refined. Furthermore, the use of a common optimum hovering rotor design for both isolated and ducted configurations is likely not an appropriate blade geometry selection. A unique propeller - or perhaps more appropriately a fan assembly - could be designed to match the thrust condition and solidity of the open propeller system, in order to make a more appropriate comparison. Additional design work can include in the incorporation of stator blades to the ducted fan assembly, as well as acoustic liners along the duct inner surface for radiated noise suppression.

References

1. Zhang, T. and Barakos, G., "Review on ducted fans for compound rotorcraft," *The Aeronautical Journal*, Vol. 124, (1277), 2020, pp. 941–974. doi: 10.1017/aer.2019.164

2. Whiteside, S. K. S. and Pollard, B. P., "Conceptual Design of a Tiltduct Reference Vehicle for Urban Air Mobility," VFS Aeromechanics for Advanced Vertical Flight Technical Meeting, San Jose, CA, January 2022.

3. Grunwald, K. J. and Goodson, K. W., "Aerodynamic Loads on an Isolated Shrouded-Propeller Configuration for Angles of Attack from -10 Deg to 110 Deg," NASA/TN D-995, NASA Langley Research Center, Hampton, VA, January 1962.

4. Mort, K. W. and Gamse, B., "A Wind-Tunnel Investigation of a 7-Foot-Diameter Ducted Propeller," NASA/TN D-4142, NASA Ames Research Center, Moffett Field, CA, August 1967.

5. Black, D. M., Wainauski, H. S., and Rohrbach, C., "Shrouded propellers - A comprehensive performance study," 5th Annual Meeting and Technical Display, AIAA Paper 1968-994, Philadelphia, PA, October 1968. doi: 10.2514/6.1968-994

6. Motsinger, R. and Kraft, R. E., *Aeroacoustics of Flight Vehicles: Theory and Practice*, NASA Langley Research Center, first edition, (1991), Chapter 14: Design and Performance of Duct Acoustic Treatment, pp. 165–206.

7. Jones, M. G., Watson, W. R., Nark, D. M., Howerton, B. M., and Brown, M. C., "A Review of Acoustic Liner Experimental Characterization at NASA Langley," NASA/TP 2020-220583, NASA Langley Research Center, Hampton, VA, April 2020.

8. Leishman, J. G., *Principles of Helicopter Aerodynamics*, Cambridge University Press, New York, NY, 2000.

9. Protolabs, Inc., "PA12 Mineral-Filled (PA620-MF)," https://www.protolabs.com/services/3d-printing/plastic/nylon/pa12-mineral-filled/, Accessed May 21, 2025.

10. Graf, W., Fleming, J., and Ng, W., "Improving Ducted Fan UAV Aerodynamics in Forward Flight," 46th AIAA Aerospace Sciences Meeting and Exhibit, AIAA Paper 2008-430, Reno, NV, January 2008. doi: 10.2514/6.2008-430

11. Martin, P. and Tung, C., "Performance and Flowfield Measurements on a 10-inch Ducted Rotor VTOL UAV," Proceedings of the American Helicopter Society (AHS) International Forum 60, Baltimore, MD, June 2004.

12. Pereira, J. L., *Hover and Wind-Tunnel Testing of Shrouded Rotors for Improved Micro Air Vehicle Design*, Ph.D. thesis, University of Maryland, College Park, MD, August 2008.

13. Fleming, J., Jones, T., and Ng, W., "Improving Control System Effectiveness for Ducted Fan VTOL UAVs Operating in Crosswinds," 2nd AIAA "Unmanned Unlimited" Conference and Workshop & Exhibit, AIAA Paper 2003-6514, San Diego, CA, September 2003.

14. Martin, P. B. and Boxwell, D. A., "Design, analysis and experiments on a 10-inch ducted rotor VTOL UAV," Proceedings of the American Helicopter Society (AHS) International Specialists Meeting on Unmanned Rotorcraft: Design, Control and Testing, Chandler, AZ, January 2005.

15. Guo, J., Zhou, T., Fang, Y., and Zhang, X., "Experimental study on a compact lined circular duct for small-scale propeller noise reduction," *Applied Acoustics*, Vol. 179, 2021.
doi: https://doi.org/10.1016/j.apacoust.2021.108062

16. Black, D. and Wainauski, H., "Hamilton Standard Shrouded Propeller Test Program, Vol I-IV," Technical report HSER 4348, Hamilton Standard, Moffett Field, CA, May 1967.

17. Whiteside, S. K. S., Zawodny, N. S., Fei, X., Pettingill, N. A., Patterson, M. D., and Rothhaar, P. M., "An Exploration of the Performance and Acoustic Characteristics of UAV-Scale Stacked Rotor Configurations," AIAA SciTech 2019 Forum, AIAA Paper 2019-1071, San Diego, CA, January 2019.
doi: https://doi.org/10.2514/6.2019-1071

18. Doty, M. J., Fuller, C. R., Schiller, N. H., and Turner, T. L., "Active Noise Control of Radiated Noise from Jets," NASA/TM 2013-218041, NASA Langley Research Center, Hampton, VA, September 2013.

19. Weitsman, D., Stephenson, J. H., and Zawodny, N. S., "Effects of flow recirculation on acoustic and dynamic measurements of rotary-wing systems operating in closed anechoic chambers," *Journal of the Acoustical Society of America*, Vol. 148, (3), 2020, pp. 1325–1336.
doi: 10.1121/10.0001901

20. Simonich, J. C., Schlinker, R. H., and Amiet, R. K., "Experimental Assessment of Helicopter Rotor Turbulence Ingestion Noise in Hover," NASA/CR 181792, United Technologies Research Center, East Hartford, CT, June 1989.

21. Brentner, K. and Farassat, F., "Modeling aerodynamically generated sound of helicopter rotors," *Progress in Aerospace Sciences*, Vol. 39, Apr 2003, pp. 83–120.
doi: https://doi.org/10.1016/S0376-0421(02)00068-4

22. Zawodny, N. S., Boyd, Jr., D. D. and Burley, C. L., "Acoustic Characterization and Prediction of Representative, Small-Scale Rotary-Wing Unmanned Aircraft System Components," AHS International 72nd Annual Forum, West Palm Beach, FL, May 2016.

23. Zawodny, N., Pettingill, N., Lopes, L., and Ingraham, D., "Experimental Validation of an Acoustically and Aerodynamically Optimized UAM Proprotor - Part 1: Test Setup and Results," NASA/TM 20220015637, NASA Langley Research Center, March 2023.

24. Thurman, C., Boyd, D. D., and Lopes, L. V., "Prediction of Broadband Blade-Wake Back-Scatter Noise from a Hovering Ideally Twisted Rotor using OVERFLOW2-ANOPP2," AIAA SCITECH 2024 Forum, AIAA Paper 2024-2471, Orlando, FL, January 2024.
doi: https://doi.org/10.2514/6.2024-2471

25. Pettingill, N. A., Zawodny, N. S., Thurman, C., and Lopes, L. V., "Acoustic and Performance Characteristics of an Ideally Twisted Rotor in Hover," AIAA SCITECH 2021 Forum, AIAA Paper 2021-1928, Virtual Event, January 2021.
doi: https://doi.org/10.2514/6.2021-1928

26. Nguyen, L. C. and Kelly, J. J., "A Users Guide for the NASA ANOPP Propeller Analysis System," NASA/CR 4768, Lockheed Engineering & Sciences, Hampton, VA, 1997.

27. Drela, M. and Youngren, H., *Axisymmetric Analysis and Design of Ducted Rotors*, Available Online: https://web.mit.edu/drela/Public/web/dfdc/DFDCtheory12-31.pdf, December 2005.

28. Farassat, F., "Linear Acoustic Formulas for Calculation of Rotating Blade Noise," *AIAA Journal*, Vol. 19, (9), Sep 1981, pp. 1122–1130.
doi: https://doi.org/10.2514/3.60051

29. Farassat, F., "Derivation of Formulations 1 and 1A of Farassat," NASA/TM 2007-214853, NASA Langley Research Center, Hampton, VA, 2007.

30. Weir, D. S., Jumper, S. J., Burley, C. L., and Golub, R. A., "Aircraft Noise Prediction Program Theoretical Manual: Rotorcraft System Noise Prediction System (ROTONET)," NASA/TM 83199, Lockheed Engineering & Sciences, Hampton, VA, 1995.

31. Lopes, L. V. and Burley, C. L., "ANOPP2 User's Manual: Version 1.2," NASA/TM 2016-219342, NASA Langley Research Center, Hampton, VA, 2016.

32. Blake, J. D., Thurman, C. S., Zawodny, N. S., and Lopes, L. V., "Broadband Predictions of Optimized Proprotors in Axial Forward Flight," AIAA AVIATION 2023 Forum, AIAA Paper 2023-4183, San Diego, CA, June 2023.
doi: https://doi.org/10.2514/6.2023-4183

33. Brooks, T. F., Pope, D. S., and Marcolini, M. A., "Airfoil Self-Noise and Prediction," NASA/RP 1218, NASA Langley Research Center, Hampton, VA, 1989.

34. Amiet, R. K., "Noise Produced by Turbulent Flow Into a Rotor: Theory Manual for Noise Calculation," NASA/CR 181788, United Technologies Research Center, East Hartford, CT, June 1989.

35. Stephenson, J. H., Weitsman, D., and Zawodny, N. S., "Effects of flow recirculation on unmanned aircraft system (UAS) acoustic measurements in closed anechoic chambers," *The Journal of the Acoustical Society of America*, Vol. 145, (3), March 2019, pp. 1153–1155.
doi: https://doi.org/10.1121/1.5092213

REPORT DOCUMENTATION PAGE

Form Approved
OMB No. 0704–0188

1. REPORT DATE *(DD-MM-YYYY)*	2. REPORT TYPE	3. DATES COVERED *(From - To)*
01-09-2025	Technical Memorandum	

4. TITLE AND SUBTITLE
Aerodynamic and Acoustic Characterization of a Ducted Propeller in a Small Hover Anechoic Chamber

5a. CONTRACT NUMBER

5b. GRANT NUMBER

5c. PROGRAM ELEMENT NUMBER

6. AUTHOR(S)
Nikolas S. Zawodny, Noah H. Schiller, Nicole A. Pettingill, and Glenn L. Medina

5d. PROJECT NUMBER

5e. TASK NUMBER

5f. WORK UNIT NUMBER

7. PERFORMING ORGANIZATION NAME(S) AND ADDRESS(ES)
NASA Langley Research Center
Hampton, Virginia 23681-2199

8. PERFORMING ORGANIZATION REPORT NUMBER
L–12456

9. SPONSORING/MONITORING AGENCY NAME(S) AND ADDRESS(ES)
National Aeronautics and Space Administration
Washington, DC 20546-0001

10. SPONSOR/MONITOR'S ACRONYM(S)
NASA

11. SPONSOR/MONITOR'S REPORT NUMBER(S)
NASA/TM–20250009190

12. DISTRIBUTION/AVAILABILITY STATEMENT
Unclassified-Unlimited
Subject Category 71, 02
Availability: NASA STI Program (757) 864-9658

13. SUPPLEMENTARY NOTES
An electronic version can be found at http://ntrs.nasa.gov.

14. ABSTRACT

This study investigates the aerodynamic performance and acoustic characteristics of a sub-scale ducted propeller relative to an open propeller of common geometry for static hover and low-speed axial flow conditions. The propeller test article is a four-bladed modified optimum hovering rotor, while the duct consists of a blended geometry between a referenced leading edge design and a NACA 0018 trailing edge. Low-fidelity modeling tools are leveraged to provide a predictive comparison for both isolated and ducted propeller systems. The ANOPP-PAS code was found to model the fundamental acoustic blade passage frequency directivity of the isolated propeller quite well, with adjustments made to the simulation case to account for additional torque loading believed to be due to "over-tripping" of the blades. Both momentum theory and the Ducted Fan Design Code yielded good agreement with the measured thrust levels of the ducted propeller system in hover, with the latter prediction method showing good agreement for low-speed axial flow conditions as well. These good agreements, however, were limited to the higher tested propeller rotation rates. Overall, the ducted propeller exhibited slightly improved propulsive efficiency in hover, and poorer efficiency in low-speed axial flow relative to the isolated propeller. Acoustically, the ducted configuration was seen to exhibit acoustic shielding at the propeller blade passage frequency, however an increase in higher blade passage frequency harmonics was also observed. There was also an increase in measured broadband noise associated with the incorporation of the duct, which was more prevalent for the hover operating conditions.

15. SUBJECT TERMS
ducted propeller, aeroacoustics, urban air mobility

16. SECURITY CLASSIFICATION OF:			17. LIMITATION OF ABSTRACT	18. NUMBER OF PAGES	19a. NAME OF RESPONSIBLE PERSON
a. REPORT	b. ABSTRACT	c. THIS PAGE			STI Information Desk (help@sti.nasa.gov)
U	U	U	UU	62	19b. TELEPHONE NUMBER *(Include area code)* (757) 864-9658